Shape defect analysis from volumetric data - Application to lattice struts in additive manufacturing

Marc-Antoine de Pastre, Yann Quinsat, Claire Lartigue

Shape defect analysis from volumetric data - application to lattice struts in additive manufacturing

Marc-Antoine de Pastre*[1], Yann Quinsat[1], and Claire Lartigue[1]

[1]LURPA, ENS Paris-Saclay, Université Paris-Saclay, 91190 Gif-sur-Yvette, France.

Abstract

Additive manufacturing (AM) revolutionises the way parts are produced as it offers a variety of design freedom. Lattice structures are an illustration of this AM freedom, allowing for the production of complex geometries that are being investigated in many applications. However, lattice structures present different typology of defects such as surface quality, porosity or dimensional inaccuracies. The most adapted measurement technology to reveal AM internal defects falls into X-ray computed tomography (XCT). Although there have been significant efforts in modelling lattice structure defects from XCT, a direct and accurate link between volumetric data of the part being measured and the CAD model is still required. This direct link would have the noteworthy advantage of not involving XCT surface determination tool, which choice may be discussed. In this paper, shape defects from metal laser powder bed fusion (PBF) strut-based lattice structures are studied. Different struts are printed as representative of BCCz lattice cells. Struts are successively measured by XCT and focus variation (FV). A virtual volume correlation (V2C) method is presented where shape defect contained in XCT volumetric data is successively approached by modal decomposition relying on a generated defect basis. The modal decomposition approach is firstly validated by comparing its efficiency towards least square cylinder approximation. Then, correlation intrinsic parameters are found, by conducting 2-dimensional sensitivity studies to identify optimal V2C parameters. V2C is further applied to the entire XCT measurements for each considered strut. Comparisons between correlated envelopes and registered FV and XCT measurements are performed to numerically estimate RMS errors. Results show that RMS errors between correlated envelopes and registered measurements are in the same order as the XCT resolution. Conclusions can then be drawn regarding the ability of V2C to estimate lattice strut shape defect relying on an user-defined shape defect basis.

Keywords: computed tomography, virtual volume correlation, modal decomposition, shape defect identification

1 Introduction

As opposed to subtractive or formative manufacturing methods, additive manufacturing (AM) techniques allow for the production of both internal and external complex geometries [1, 2]. Indeed, within a wide scope of applications, designers and engineers can optimise geometries in order to reduce weight for a given load, to strengthen the part mechanical properties [3, 4] or to improve a cooling process through new heat exchangers [5, 6]. As a particular advantage of AM, strut-based lattice structures are increasingly being studied for their inherent properties such as resulting porosity or mechanical stiffness [7, 8, 9, 10]. These structures consist of an elementary pattern, generally called an unit cell, regularly repeated in all directions to form a network [7, 11, 12]. However, the manufacturing step introduces defects into the resulting part. In this paper, the powder bed fusion (PBF) process [13] will be specifically addressed. Previous work highlights such defects and identify their contributing parameters for PBF [14, 15]. As a summary, defects affecting PBF AM parts have been reviewed and classified into four types by Malekipour and El-Mounayri [16]: geometrical and dimensional defects, surface quality, micro-structure defects and defects affecting the part mechanical properties. Focusing on the geometrical and dimensional defects, Malekipour and El-Mounayri propose a decomposition by form and size defects. However, this consideration is not unique and with the same four-type classification as Malekipour and El-Mounayri, Vo et al. [17] propose another decomposition for the geometrical and dimensional defects consisting in inaccuracy and deformation. As reviewed in [7] for PBF, lattice structure defects are considered onto a three-fold characterisation: dimensional inaccuracies (such as strut diameter deviation), surface defects and porosity. Dimensional inaccuracies for lattice structures are challenging to investigate, as it raises the question of scale. Indeed, dimensional defects affecting lattice structure are twofold: defects at the scale of the strut within the structure and defects of the overall structure. Both of these scales are then connected as the overall

*Corresponding author: Marc-Antoine de Pastre, email address: marc-antoine.de_pastre@ens-paris-saclay.fr

structure dimensional defects may result in the sequence of local strut dimensional defects. Although there have been recent work in modelling lattice structure defects [18, 19, 20, 21, 22, 23, 24], efforts are still required to improve a direct link between volumetric data of the part being measured and the CAD model. In order to pursue industrial development and take full advantage of the benefits of additive manufacturing processes, it is necessary to control the geometry of produced parts and to characterise observed defects [25, 26]. Measurement methods now focus on X-ray computed tomography (XCT) for its ability to reconstruct internal structures and to assess dimensional deviations [7, 27]. In fact, XCT consists in projecting X-rays all around the measured sample where volumetric reconstruction is then performed by dedicated algorithms [28]. As reviewed by Thompson *et al.* [29], a significant bulk of work has been performed to compare XCT measurements of additive lattice structures with the original CAD model. Nevertheless, XCT measurement uncertainty depends on various parameters. Kim *et al.* [30] investigated different XCT measurement parameters to highlight the impact on both noise and probability of defect detection. Rathore *et al.* [31] particularly focused on XCT resolution and measuring conditions applied to lattice structures, evaluating measurement deviations towards the nominal model. Rodríguez-Sánchez *et al.* reviewed the influence of noise on the resulting measurement uncertainty [32]. Recent work particularly addressed the metrological traceability in XCT measurements for metal AM lattice structures, developing the substitution method for dimensional assessments [33, 34].

All dimensional measurements using XCT are based on the material boundary determination relying on thresholding [35]. Significant efforts have been made to reduce uncertainty in edge determination by subvoxel investigations in order to numerically improve resolution [36, 37]. Hence, it has been shown in an intercomparison of different tomography instruments [38], that a measurement uncertainty of the order of 1/10 of the initial voxel size can be obtained by a subvoxel study. Traditionally, surface extraction algorithms are applied on volumetric data such as $ISO_{50\%}$ [39] or gradient-based methods [40]. However, literature shows that according to the chosen surface extraction criteria, discrepancies may be observed [39, 41, 42]. In addition, exporting extracted surfaces may be a prolonged task due for example to the required meshing time prior to CAD import. In the CAD software, a final registration step would be necessary towards the nominal part, before performing any dimensional assessment on the measured part relative to the nominal part. That is why, this data pipeline may result in a lengthy task, with successive operations depending on user parameters (such as surface extraction tool choice, mesh size or registration criteria). These difficulties are described by López and Vila [43] who noted the absence of surface reconstruction standard procedure for AM. Efforts are then required to narrow the link between CAD model and XCT, restraining any uncertainty source, to provide the CAD model with an updated geometry based on XCT measurement. Such CAD model update can be of interest for integrating shape defect in future design or to conduct dimensional specification studies on the measured part.

Alternatively, recent work has shown the interest of correlation techniques in the contour identification and extraction in various applications. More precisely, virtual image correlation (VIC) techniques have been introduced. VIC basically deals with two images: a first one specified as physical (referring to its physical measurement origin) and a second one designated as a virtual one (referring to its virtual construction) [44]. Contour determination contained in the physical image is performed by successively deforming the virtual image contour in order to minimise grey level differences between both physical and virtual images. In other words, VIC consists in finding the digital analytical contour, which best fits the physical contour, by iteratively deforming digital modelling. It is worth noting that VIC is different from digital image correlation (DIC) since DIC uses two physical images: a reference and a deformed one [45]. For example, DIC is of interest for Young modulus calculations, extracting deformation field from images successively acquired during tensile test. Although VIC has not been studied to the same depth than DIC, there has been some work that focused on medical and mechanical application of VIC. In most publications, VIC has been applied in 2-dimensional (2D) studies. In mechanical field, Rhétoré *et al.* [25] relied on B-spline contour modelling in order to analyse a high temperature mechanical testing. What's more, François *et al.* and Semin *et al.* [44, 46] addressed the DIC limitation by VIC for large, elongated and curved structures for shape boundary identification. Indeed, for DIC to be efficient, a speckle pattern must be spread over the part being studied. For slender structures, such a pattern would not be visible on physical images. That is why, authors highlight the efficiency of VIC to precisely identify shape boundary which can then be implemented into a bending profile study. Using the same approach, Bloch *et al.* [47] have performed VIC to monitor inflatable structures evolution in a material strength comparative study of Euler-Bernoulli and Timoshenko hypothesis. Authors notably highlight the precision advantage of VIC in comparison to other edge detection methods, in addition to its ease of implementation. Moreover, it has been proven that correlation of virtual images allows shape contour determination with a better resolution than the measured data [25]. However, as Bloch *et al.* [47] highlight, VIC methods are limited to laboratory brightness and contrast conditions to precisely monitor shape evolution for example. On a numerical aspect, VIC consists in a matrix pseudo-inversion with potential conditioning issues. In the medical field, VIC

has been shown of interest for the reconstruction of digital pelvic organs. For example, VIC is applied in 2D [48] and in 3-dimensional (3D) [49] approaches. In these applications, geometric modelling of pelvic organs from magnetic resonance imaging (MRI) scans allows specific pathology to be identified from reconstructed digital models in order to provide the patient with adapted treatment. More accurately, both of these investigations rely respectively on B-spline curve [48] and NURBS surface [49] for their continuity properties to describe respectively virtual contour (2D) and virtual envelope (3D).

Despite this notable interest in contour analysis and thus the processing of volumetric data from tomography, virtual correlation methods remain underdeveloped. Indeed, as highlighted by François *et al.* [44], many physics or engineering fields rely on defining the object shape by edge detection whose techniques are reviewed elsewhere [50, 51, 52, 53]. With virtual correlation, envelope is described by analytical expression which can be easily implemented into a digital representation.

Strut-based lattice structures are nominally cylindrical. However, due to the manufacturing step, produced struts are not cylindrical anymore but embedded with shape defects. A first order shape defect approach would approximate these shape defects as ellipses [8, 54]. Considering strut measurement as point cloud, each of these points is projected into a plane defined by the associated least square cylinder axis [55]. However, this first order approximation is not sufficient to completely describe and characterise the shape defect generated during the manufacturing step and to validate structure performance [56]. As a solution to this limitation, Samper *et al.* [57] present a modal decomposition of shape defect using a finite element approach to identify the defect basis. More precisely, shape defect is decomposed of several elementary participations, whose sum best fits the observed defect. Authors argue that modal participation amplitude decreases with high frequency, which means that computing the entire defect basis should not be necessary to precisely approximate shape defects. As an illustration, Thiebault *et al.* [58] use this decomposition method to identify thin part shape defects. In addition, Homri *et al.* [59] noted the modal decomposition usefulness for cylinder shape defect identification and for its implementation into part geometrical definition and tolerancing. This methodology may be used to separate roughness from form defect, as shown in previous work [60].

Nevertheless, recent work has proposed a modal approach for shape defect measurement relying on DIC [61]. Such method allows shape defects to be digitally modelled assuming that the built modal basis is sufficiently representative of defects range. Indeed, modelling strut-based lattice structure shape defects in digital representation would allow the CAD model of the produced lattice part to be updated, taking into account these measured defects.

That is why, virtual correlation creates a connecting link between the real part geometry and its CAD model. In other words, virtual correlation has the advantage of involving neither XCT surface determination tool nor successive user-dependant steps that may introduce uncertainty. With virtual correlation, the nominal model is directly updated relying on volumetric data.

In this paper, efforts have been focused on developing a virtual volume correlation (V2C) method allowing direct identification of shape defects from volumetric data, relying on modal decomposition. In other words, this paper presents a shape defect identification methodology directly from volumetric data, without any post-reconstruction data treatment step. Particular attention will be paid to dimensional shape defects of additively manufactured PBF lattice structures, measured by XCT. This paper is organised as follows: Section 2 presents the V2C mathematical methodology and how it can be applied on volumetric data. More precisely, this section describes the considered basis used to approximate strut shape defects. Section 3 describes experimental acquisitions and highlights the suitability of the modal decomposition towards least square approximations. More precisely, in this section, V2C relevancy towards the chosen shape defect basis is discussed. In Section 4, the V2C optimal parameter setup is estimated and a sensitivity study through easy-to-compute examples is performed. When optimal parameters are found, V2C is applied on volumetric data in Section 5. Finally, consistency of V2C and the chosen modal basis is studied on spatially repeated struts and measurement repeatability study is performed to evaluate the measurement uncertainty impact on V2C. Discussion is then proposed regarding the considered shape defect basis and the integration of repeatability notions. On a computing aspect, required numeric resources are also outlined.

2 Methodology

2.1 Mathematical considerations

In XCT scans, grey level histograms depict two main peaks: a bright one for the irradiated material and a dark one for the surrounding background. Transition between bright and dark areas is a voxel bandwidth which contains contour information. In the V2C method, measured part contour is analytically expressed in a digital modelling. More precisely, XCT measurements define a physical volume whilst virtual volume is generated by minimising grey level errors in comparison to this so called physical volume. This method is particularly adapted to closed-loop geometries [25].

Several mathematical writings have been proposed in previous work [25, 46, 48, 49] for the VIC method. In this paper, we present the V2C method, extending the VIC method to 3D volumes. Physical volume, stemming from measurements, is considered as undeformable and displacement fields are applied on the virtual volume to best fit the physical volume.

Let f be a physical volume. This volume contains a closed envelope embedded with shape defect that can be expressed as a displacement field $\mathbf{u}$ to be identified. Let $\{\mathbf{X}_f\}$ be the voxels defining that envelope. Similarly, let g be a virtual volume and $\{\mathbf{X}_g\}$ the voxel defining the virtual envelope and $\{\mathbf{n}_g\}$ the associated local normal vectors taken according to the exterior material convention. Initially, the virtual volume contains the original regular shape. Each point of the physical envelope can be written as:

$$\mathbf{X}_f = \mathbf{X}_g + \mathbf{u} \tag{1}$$

The V2C method consists in minimising grey level differences between physical and virtual volumes relying on a least square criterion. A correlation score Φ should be introduced as:

$$\Phi = \iiint_{\mathrm{ROI}} \left[f(\mathbf{X}) - g(\mathbf{X}+\mathbf{u})\right]^2 d\Omega \tag{2}$$

where ROI refers to the region of interest in terms of considered voxels and $\{\mathbf{X}\}$ refers to considered voxels in the physical volume f. Displacement field $\mathbf{u}$ only applies on the virtual contour points and can be described as a sum of elementary displacement fields:

$$\mathbf{u} = \sum_k \lambda_k \mathbf{u}_k \tag{3}$$

Where λ_k are the components of $\{\boldsymbol{\lambda}\}$ and refer to the intensity of the elementary displacement description $\mathbf{u}_k$. Displacement field will be chosen according to the investigated geometry and will be discussed in Section 2.3.
Back in equations 1 and 2:

$$\mathbf{X}_f = \mathbf{X}_g + \sum_k \lambda_k \mathbf{u}_k \tag{4}$$

and

$$\Phi(\boldsymbol{\lambda}) = \iiint_{\mathrm{ROI}} \left[f\left(\mathbf{X}\right) - g\left(\mathbf{X} + \sum_k \lambda_k \mathbf{u}_k\right)\right]^2 d\Omega \tag{5}$$

whose formulations should be simplified as:

$$\mathbf{X}_f = \mathbf{X}_g + \lambda_k \mathbf{u}_k \tag{6}$$

$$\Phi(\boldsymbol{\lambda}) = \iiint_{\mathrm{ROI}} \left[f\left(\mathbf{X}\right) - g\left(\mathbf{X} + \lambda_k \mathbf{u}_k\right)\right]^2 d\Omega \tag{7}$$

Let $\{\boldsymbol{\lambda}^*\}$ be the vector containing all elementary displacement intensities and defined as:

$$\{\boldsymbol{\lambda}^*\} = \underset{\{\boldsymbol{\lambda}\}}{\arg\min}\, \Phi(\mathbf{u}) \tag{8}$$

A first order linearisation of equation 7 leads to:

$$\Phi_{\mathrm{lin}}(\lambda) = \iiint_{\mathrm{ROI}} [f(\mathbf{X}) - g(\mathbf{X} + \lambda_k \mathbf{u}_k) - \Delta\lambda_j \nabla g(\mathbf{X} + \lambda_k \mathbf{u}_k).\mathbf{u}_j]^2 d\Omega \tag{9}$$

The minimisation of the score of correlation Φ_{lin}, in application of a Gauss-Newton scheme, gets to:

$$\underline{\underline{M}}.\boldsymbol{\Delta\lambda} = \mathbf{b} \tag{10}$$

with

$$M_{ij} = \iiint_{\mathrm{ROI}} \nabla g(\mathbf{X} + \lambda_k \mathbf{u}_k).\mathbf{u}_j \times \nabla g(\mathbf{X} + \lambda_k \mathbf{u}_k).\mathbf{u}_i d\Omega \tag{11}$$

and

$$b_i = \iiint_{\mathrm{ROI}} \left[f(\mathbf{X}) - g(\mathbf{X} + \lambda_k \mathbf{u}_k)\right] \nabla g(\mathbf{X} + \lambda_k \mathbf{u}_k).\mathbf{u}_i d\Omega \tag{12}$$

In other words, V2C method can be condensed into a linear equation (see equation 10) that allows $\boldsymbol{\Delta\lambda}$ to be identified. For the first order linearisation reason, V2C is an iterative procedure, identifying $\boldsymbol{\Delta\lambda}$ that is used to update the virtual volume. Minimisation is then repeated until convergence, where the sum of all iterative $\boldsymbol{\Delta\lambda}$ tends to $\{\boldsymbol{\lambda}^*\}$. A note should be made about mathematical considerations which can be deduced from this expression. Firstly, by application of the Gauss-Newton method, V2C results in an iterative procedure to find the correlated volume. Each iteration step consists of a small virtual volume displacement which tends to minimise the correlation score Φ. That is why, V2C can easily be implemented into algorithm procedure, where amplitudes of displacement field are found from the mathematical pseudo-inversion of equation 10. However, the latter raises conditioning issues (ratio between lowest and highest eigen values of M matrix) which would require the appropriate-conditioning of our problem.
As assumed in the beginning of this section, the physical volume f is found to be kept undeformable as physical volume is only considered in equation 12, without any applied displacement field. Moreover, a gradient is introduced in equation 9 by developing the Gauss-Newton method. Gradient only applies on the iteratively-modified virtual volume. As composed of grey values scaled from 0 (surrounding virtual backgound) to 1 (virtual material), gradient explicitly expresses the voxel bandwidth transition and gradient is valued to 0 out of the transition bandwidth.

To sum up, V2C iteratively applies a displacement field on a virtual volume whose amplitude is expressed

by inversion of equation 10. In order to numerically implement V2C method, an initial virtual volume has to be defined.

2.2 Generation of initial virtual volume

Initial virtual volume consists in the nominal envelope that should be iteratively deformed by V2C until it matches the physical volume. More precisely, initial virtual volume is generated by levelset methodology [25, 62] from an original reference shape. The main stake of V2C is to define the virtual voxel bandwidth R_g grey levels in each virtual volume to generate. In the following, white level (resp. black level) is associated to 1 (resp. 0) grey value. Let $\{\mathbf{x}_i\} = \{x_i, y_i, z_i\}$ be the original reference shape closed-envelope voxel coordinates and $\mathbf{X}_{cv}$ the current voxel in the virtual volume and let $\{\mathbf{n}_i\}$ be the associated envelope normals.

- If the current voxel $\mathbf{X}_{cv}$=(m,n,o) is inside the closed contour and within the $\frac{R_g}{2}$ bandwidth, then the assigned grey value I($\mathbf{X}_{cv}$) is:

$$I(\mathbf{X}_{cv}) = \frac{1}{2}\left(1 + cos\left(\pi \frac{||(\mathbf{X}_{cv} - \mathbf{x}_i).\mathbf{n}_i|| - \frac{R_g}{2}}{R_g}\right)\right) \tag{13}$$

- If the current voxel $\mathbf{X}_{cv}$=(m,n,o) is outside the closed contour but within the $\frac{R_g}{2}$ bandwidth, then the as-

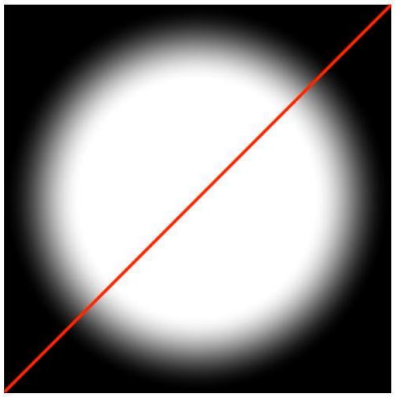

(a)

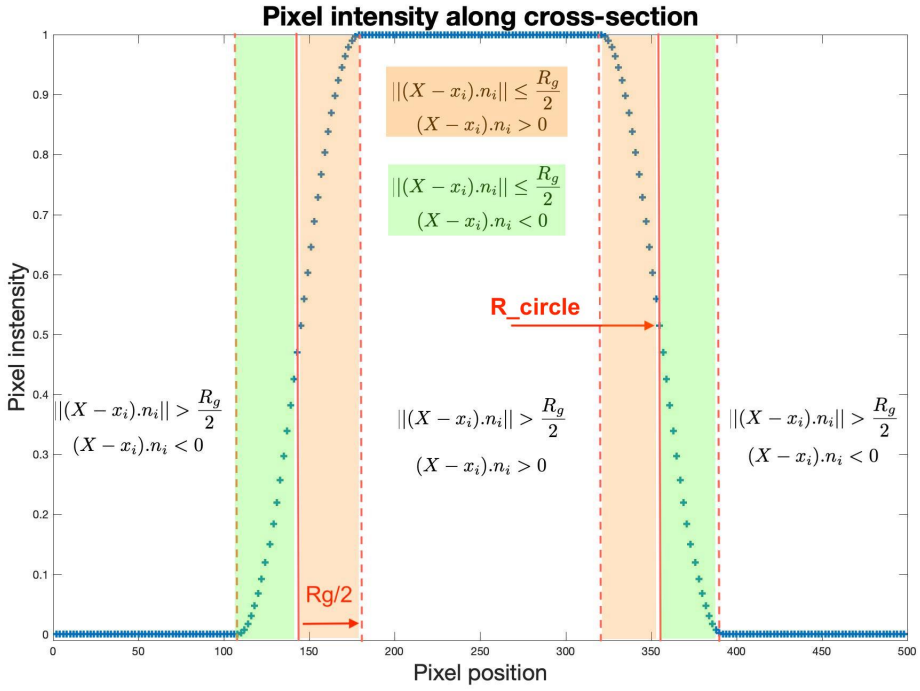

(b)

Figure 1: Cross-section example on a virtual circle initial shape (a) and the associated grey level pixel values according to the pixel position conditions regarding the original shape reference (b).

signed grey value I($\mathbf{X}_{cv}$) is

$$I(\mathbf{X}_{cv}) = \frac{1}{2}\left(1 + cos\left(\pi \frac{||(\mathbf{X}_{cv} - \mathbf{x}_i).\mathbf{n}_i|| + \frac{R_g}{2}}{R_g}\right)\right) \quad (14)$$

- If the current voxel $\mathbf{X}_{cv}$=(m,n,o) is outside the closed contour and outside the $\frac{R_g}{2}$ bandwidth, then the assigned grey value is 0

- If the current voxel $\mathbf{X}_{cv}$=(m,n,o) is inside the closed contour and outside the $\frac{R_g}{2}$ bandwidth, then the assigned grey value is 1

In order to better understand the virtual volume construction, a 2D example is provided in Figure 1. More precisely, this example summarises the pixel intensity according to the pixel position regarding the virtual original shape reference for a circular 2D example.

2.3 Shape defect basis description

In previous work, displacement field was approximated using B-splines [25, 48] or NURBS surfaces [49], whose contours are successively deformed. In this paper, as lattice structures struts are being studied, a cylindrical nominal reference shape is considered in the initial virtual volume defined by a z-axis (strut length general orientation) and a x and y-axis plane. Shape defects contained in the physical volume are expressed through modal decomposition [61]. This modal decomposition is separated in a four-part classification according to the cylindrical nature of studied struts : rigid transformations, dilatation, vertical waviness defect and plane deformations. More precisely, rigid transformations encapsulate x and y translations and rotations, dilatation refers to the radius correction, vertical waviness defines rippled modes as a sinusoidal deviation along the cylinder axis (see [59]) and plane deformations refer to the 2D x-y deformations whose description is chosen as a sinusoidal expression. In other words, with $\mathbf{X}_F$ being the envelope position in the physical volume, we may write:

Taper	Barrel	Hourglass (illustration of negative barrel)
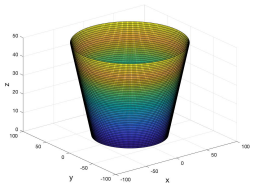	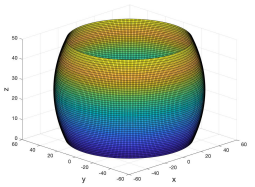	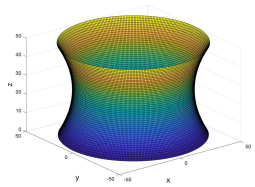
$\mathbf{u}_{taper}(x,y,z) = \begin{pmatrix} \frac{\sqrt{2}}{L} z.cos(\theta) \\ \frac{\sqrt{2}}{L} z.sin(\theta) \\ 0 \end{pmatrix}$	$\mathbf{u}_{barrel}(x,y,z) = \begin{pmatrix} \frac{4}{L^2} z(L-z).cos(\theta) \\ \frac{4}{L^2} z(L-z).sin(\theta) \\ 0 \end{pmatrix}$	$\mathbf{u}_{hourglass}(x,y,z) = \begin{pmatrix} \frac{4}{L^2} z(z-L).cos(\theta) \\ \frac{4}{L^2} z(z-L).sin(\theta) \\ 0 \end{pmatrix}$
Vertical defect 1	Vertical defect 2	Vertical defect 3
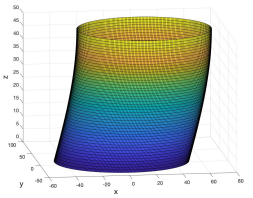	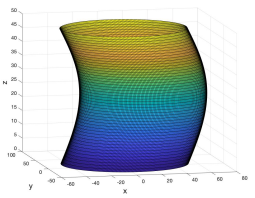	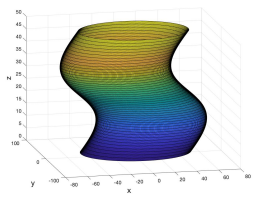
$\mathbf{u}_{vd-1}(x,y,z) = \begin{pmatrix} sin(\frac{\pi}{2L}.z) \\ sin(\frac{\pi}{2L}.z) \\ 0 \end{pmatrix}$	$\mathbf{u}_{vd-2}(x,y,z) = \begin{pmatrix} sin(2\frac{\pi}{2L}.z) \\ sin(2\frac{\pi}{2L}.z) \\ 0 \end{pmatrix}$	$\mathbf{u}_{vd-3}(x,y,z) = \begin{pmatrix} sin(3\frac{\pi}{2L}.z) \\ sin(3\frac{\pi}{2L}.z) \\ 0 \end{pmatrix}$
5^{th} mode	22^{th} mode	35^{th} mode
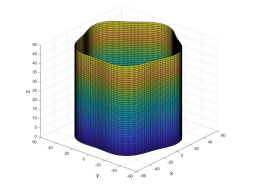	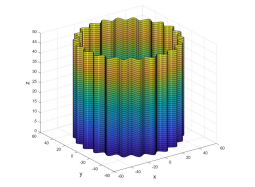	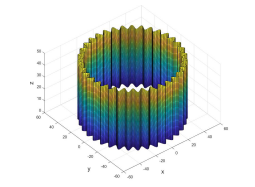
$\mathbf{u}_{pd-5}(x,y,z) = \begin{pmatrix} cos(5.\theta).cos(\theta) \\ cos(5.\theta).sin(\theta) \\ 0 \end{pmatrix}$	$\mathbf{u}_{pd-22}(x,y,z) = \begin{pmatrix} cos(22.\theta).cos(\theta) \\ cos(22.\theta).sin(\theta) \\ 0 \end{pmatrix}$	$\mathbf{u}_{pd-35}(x,y,z) = \begin{pmatrix} cos(35.\theta).cos(\theta) \\ cos(35.\theta).sin(\theta) \\ 0 \end{pmatrix}$

Figure 2: Example of considered modes (amplitudes have been manually enhanced for more readability). L refers to the strut length, and θ refers to the normal angle of each contour point.

$$\mathbf{X}_F = \mathbf{X}_0 + \mathbf{u}_{rt} + \mathbf{u}_d + \mathbf{u}_{vd} + \mathbf{u}_{pd} \tag{15}$$

Where $\mathbf{X}_0$ is the nominal strut centre and:

- $\mathbf{u}_{rt}$ refers to rigid transformation i.e. two translations along both horizontal axis and two rotations around x and y axis.
- $\mathbf{u}_d$ refers to dilatation expressed as a the global variation effect of shape radius

$$\mathbf{u}_d = \lambda_d.\mathbf{n}_g \tag{16}$$

- $\mathbf{u}_{vd}$ refers to vertical defect. More precisely, this displacement depends on the vertical position z and can be decomposed into:
  - two vertical section modification descriptors: taper and barrel modes [59] (a negative barrel is equivalent to a hourglass mode)
  - vertical rippled modes [59] described as a sum
- $\mathbf{u}_{pd}$ refers to the sinusoidal plane defects defined by

$$\mathbf{u}_{pd} = \sum_i \left[\lambda_{i,1}.cos(i\theta) + \lambda_{i,2}.sin(i\theta)\right].\mathbf{n}_g \tag{17}$$

  where $\{\theta\}$ is the contour angle defined as the center angle at each contour point with local normal $\{\mathbf{n}_g\}$.

Figure 2 illustrates some of the considered modes and their mathematical definitions.

These modes are defined by the user and their relevance towards strut shape defects is shown in the next section.

3 Experimental acquisitions and defect basis validation

In order to lead further investigation on V2C, volumetric data of laser PBF struts are required. This section describes manufacturing, measurement and processing of the samples. Shape defect basis relevance towards measured struts is particularly highlighted.

3.1 Examined samples

The samples used are representative of struts composing a BCCz lattice structure. A BCCz lattice structure is a structure made of vertical struts as well as inclined struts i.e. struts with a 45° overhang angle. These elementary struts are spatially repeated and displayed on a basement structure as shown in Figure 3, all designed in a CAD software. A physical marking was added to identify same ROI in further registrations (see Figure 3b) and to maximise the quality of alignment. Samples were designed according to spacing recommendations specified in ISO/ASTM 52902 [63] for resolution pin artefact design. More details

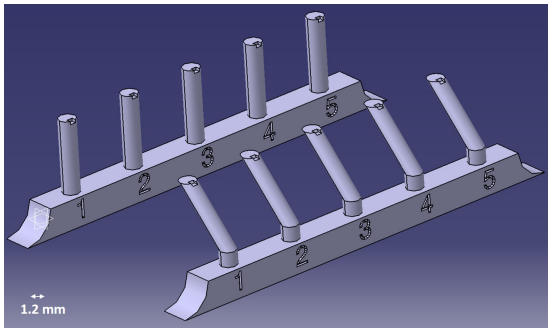

(a)

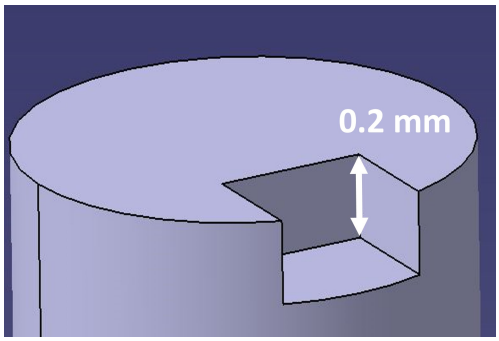

(b)

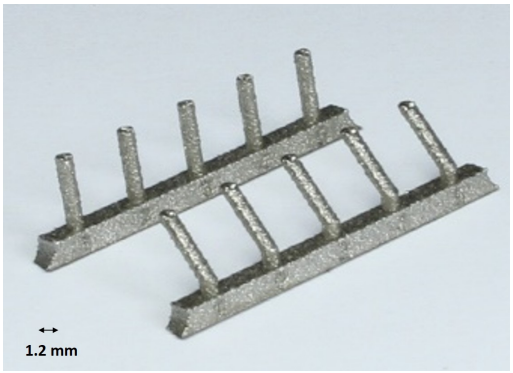

(c)

Figure 3: CAD (a) and printed (c) samples. Strut tips are marked with a 0.2 mm height marking (b) for further registration steps.

about stakes and specific AM defects to be considered in the artefact design can be found in [64]. More precisely, for both samples, struts are regularly spaced, strut radii are set to 0.6 mm, have a 5 mm length, with a 1 mm length support added for both vertical and inclined sets to push aside the strut from the basement structure. Basement size and shape have been customised by fillet-fitting to improve manufacturing conditions. Samples were produced by laser PBF ([13]) on an Addup FormUp 350 printer using Inconel 718 powder. Printing parameters were set up according to the manufacturer's guidance following parameters: layer thickness of 40 μm ; laser power of 220 W, scan speed of 2100 $mm.s^{-1}$, contour scan power of 210 W, contour scan speed of 1800 $mm.s^{-1}$, hatch spacing of 55 μm. Manufactured samples were then washed with water

and dried with compressed air. Parts were removed from the substrate using an electrical discharge machine.

3.2 Measurement setups and data processing

In the following, XCT and focus variation (FV) [65] measuring instruments are used. The relevancy of comparing data stemming from XCT and FV was shown for instance for surface texture comparisons of metal PBF in [66, 67] and for polymer PBF in [68]. Each strut was sawed to be measured separately by XCT and by FV and measurement setups for both instruments are as follows:

- XCT: Instrument: North Star Imaging X50; X-rays source: XRayWorX; Detector: Dexela 2923; Each sawed strut was displayed in a home-made tool holder, in a vertical position, to get the rotary plate plane parallel the supporting basement plane. Geometric magnification of 33 % leading to a voxel size of 9 μm. Volumetric reconstruction was performed from 900 projections (averaging of 10 exposures, each lasting 0.1 s), tube voltage 150 kV, tube current 40 µA. A warmup scan of approximately 30 minutes was performed prior to the first scan and data were reconstructed in the manufacturer's software, relying on a filtered back projection algorithm, using a beam hardening correction without specific filter. Reconstructions were saved in a .raw file format.
- FV: Alicona Sensor IF-R25, 10× objective lens with long working distance, numerical aperture 0.3, field of view (2.05 × 2.05) mm, pixel lateral resolution 2.07 μm, optical lateral resolution 0.91 μm, contrast lateral resolution 0.53 μm), coaxial illumination, stage rotation step of 50°, fusion of multiple field of views performed in the manufacturer's software, measured volume after fusion (1.3 × 1.3 × 5.6) mm. Neither form removal nor cutoff filters were applied on the measurements.

All numerical computations were performed in Matlab [69]. When needed, cloud-to-mesh distances were computed in CloudCompare [70].

3.3 Basis validation

This section aims at validating the chosen defect basis regarding the shape defect contained in lattice structure struts. Indeed, the proposed shape defect basis should provide improvements of shape defect identification in comparison to the least square cylinder for example. Prior to further investigations, the chosen basis validation is an important step in order to assess if the considered shape defect basis is relevant to the studied geometry. In the following, two struts from each sets have been selected. For each strut, the FV measurement dataset has been considered to compute the least square cylinder on the one hand. On the other hand, a non-rigid registration modal decomposition [58] is completed relying on the aforemen-

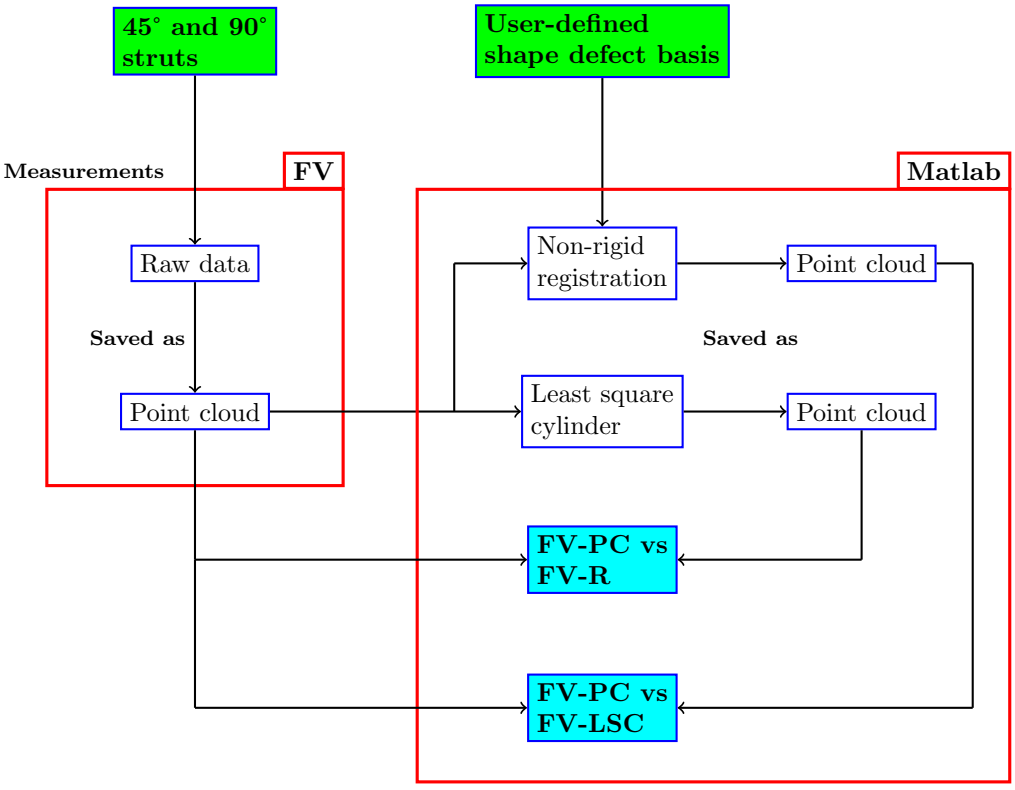

Figure 4: Data processing pipeline for basis validation. Inputs are filled in green, outputs are filled in blue. FV-PC, FV-R and FV-LSC refer respectively to FV point cloud, registered envelope and least square cylinder.

tioned shape defect basis. With the obtained modal decomposition, the strut is reconstructed. FV point cloud is compared to respectively the reconstructed strut after non-rigid registration, and to the least square cylinder. The data processing pipeline is summarised in Figure 4. Deviations corresponding to blue fills in Figure 4 are summarised in Table 1 by mean and RMS values.

	Deviation	FV PC vs FV R	FV PC vs LSC
90°	Mean (μm)	-5.8	-5.7
	RMS (μm)	18.0	19.0
45°	Mean (μm)	-8.2	-17.5
	RMS (μm)	20.0	35.9

Table 1: Comparison of mean and RMS deviations of FV point clouds (FV PC) towards respectively FV registered envelope (FV R) and least square cylinder (LSC).

For the 90° strut, there is no notable improvement using modal decomposition, instead of least square cylinder, to identify shape defect. Mean deviations are about the same values with a slight reduction of RMS deviations when using modal decomposition. This observation may be explained by two arguments. Firstly, 90° struts are strictly vertical and are not affected by tilting effects during the printing process. Secondly, the printing process includes a contour scan strategy which tends to whittle down surface defects. In laser PBF, contour scan strategy consists in the laser tracing the perimeter of enclosed material at each layer. More precisely, as explained in [71], contour scanning laser melts the surface irregularities resulting in an improved surface quality. For the 45° strut, there is a major improvement of the shape defect identification using the proposed defect basis rather than the least-square cylinder fitting. Indeed, mean deviation is lowered from -17.5 μm obtained with least square cylinder, down to -8.2 μm obtained with the registered strut. Same observations can be made with RMS deviations. In other words, the registered strut provides a more detailed strut shape defect than least square cylinder. That is why, the considered shape defect basis is relevant towards the studied geometry. Based on appropriate literature, strut shape defect are expected to be mainly cylindrical and elliptic as shown in [54]. The main advantage of using this shape defect basis is to identify further shape defect than these traditional expectations and to narrow the shape defect identification. However, this shape defect decomposition is limited by the strut roughness, which is mainly random and non-periodic along the strut [8].

4 Parameter setup and sensitivity study

V2C involves different parameters that need to be optimised to increase correlation efficiency. In this section, transition size ratio $\frac{R_g}{R_f}$ of both virtual and physical volumes, as well as number of plane modes are considered and sensitivity studies are performed on 2D application of V2C, with the aim of reducing computational costs.

4.1 2D V2C

In order to fully understand the considered method and to find optimal setup parameters within a reasonable computation time, the proposed V2C method and its modal decomposition is firstly validated on 2D cross-sectional grey level images stemming from the volume reconstruction of XCT lattice strut measurements. In this setup, the aforementioned vertical defects are not considered. Initial virtual shape consists in a circle whose radius is set to 0.6 mm, i.e. the CAD definition of lattice strut radius, and whose initial position is thoughtfully chosen by the user to limit the need for registration. Analytical virtually-computed contours are compared to the extracted $ISO_{50\%}$ contour [39, 72] using Fiji software [73]. Although there are ongoing discussions about surface determination tool accuracy over another [39, 41, 42], $ISO_{50\%}$ surface determination tool was chosen over gradient-based methods for better reproducibility of this work. In fact, gradient-based are mainly proprietary software black boxes where parameters cannot be easily checked, whereas $ISO_{50\%}$ can be easily implemented. Mean and RMS errors are computed according to the number of considered modes. A comprehensive study of the modal decomposition is provided to fully understand the impact of the number of modes considered on the computed and extracted contour discrepancies. Indeed, computation of eigenvalues via the Hessian description allows influential shape defect modes to be identified [61]. Illustration of the fitting process via the 2D V2C is highlighted in Figures 5 and 6 comparing the measured image with initial and correlated virtual images.

4.2 Parametric sensitivity

The 2D validation of the proposed V2C method is used to find the best parameters for the problem description of both struts. Main correlation parameters to optimise are $\frac{R_g}{R_f}$ ratio and the number of plane modes. Previous work [25] has identified the $\frac{R_g}{R_f}$ ratio set to 1 as optimal with B-splines displacement descriptors and the undertaken studies of this paper conformed to that result. Thereby, in the following, the sensitivity study is performed on the number of plane modes under the condition of $\frac{R_g}{R_f} = 1$. This sensitivity study is performed for 2D cross-sections and then does not consider vertical modes. The optimal number of vertical modes to consider in 3D V2C will be addressed in Section 4.3, by assuming an initial number of vertical modes and confronting that assumption to estimated modal amplitudes. Comparisons of mean and RMS errors between virtually computed contour and extracted $ISO_{50\%}$ contour (see data pipeline in Figure 7) are presented in Figure 8. Results show similar trends in the mean and RMS errors according to the mode number

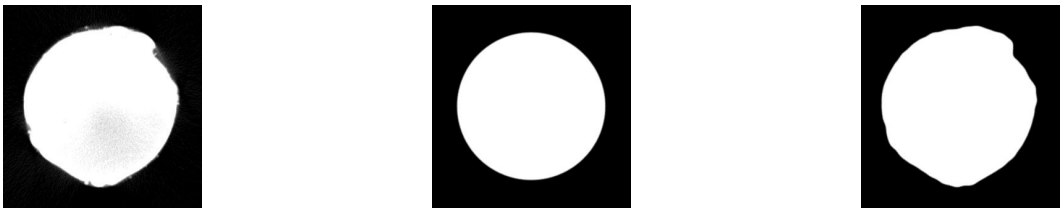

(a) (b) (c)

Figure 5: Illustration of 2D V2C method for the vertical 90° strut: CT measurement image (a), initial virtual shape (b) and correlated final virtual shape (c)-(image size (332×330) pixels, 61 considered plan defect modes, $\frac{R_g}{R_f} = 1$, 89 iterations).

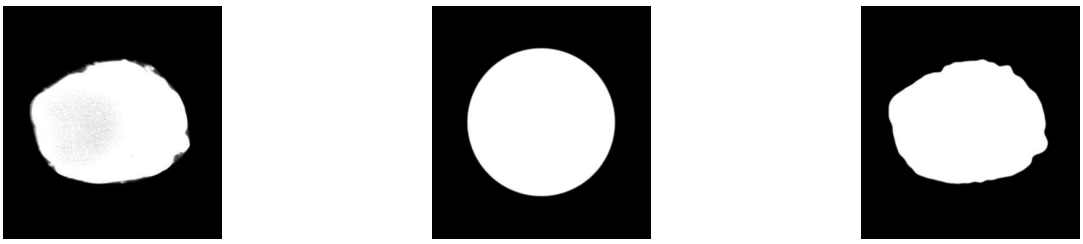

(a) (b) (c)

Figure 6: Illustration of 2D V2C method for the 45° strut: CT measurement image (a), initial virtual shape (b) and correlated final virtual shape (c)-(image size (378×356) pixels, 61 considered plan defect modes, $\frac{R_g}{R_f} = 1$, 147 iterations).

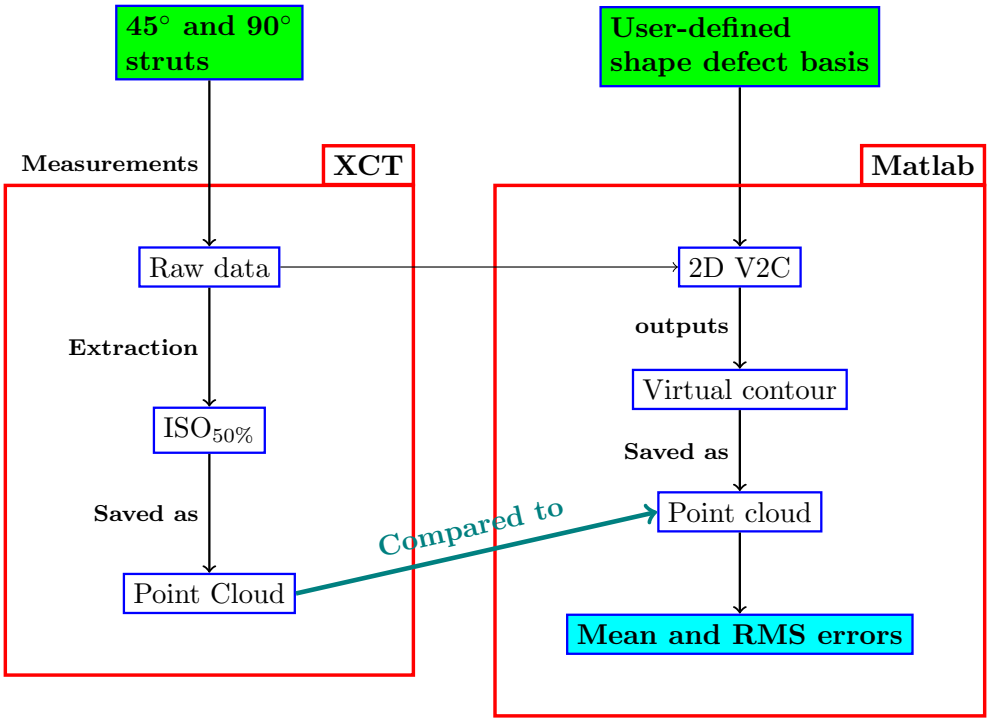

Figure 7: Data processing pipeline for 2D V2C. Inputs are filled in green, outputs are filled in blue.

taken into consideration. Several modes are considered in the shape defect basis in order to cover up sufficiently different shape defects. Figure 9 represents each of the modal participation by plotting the mode amplitudes at the end of the correlation process using the optimal parameters previously mentioned. Figure 10 depicts two of the considered modes. As also shown in Figure 8, the number of considered modes in the shape defect description also impacts the resulting error. Indeed, it seems logical that numerous modes provide a deeper

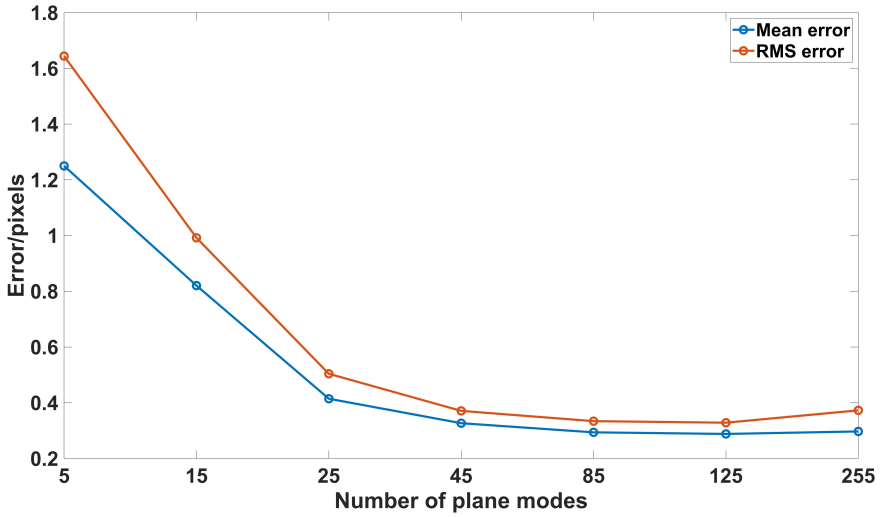

(a) 90° strut

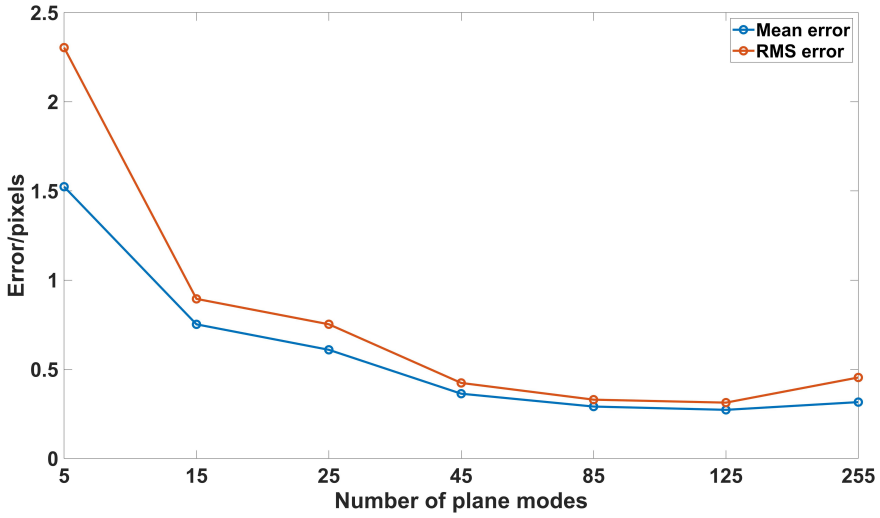

(b) 45° strut

Figure 8: Comparison of mean and RMS errors between correlated contour and $ISO_{50\%}$ contour according to the number of considered plane modes and with $\frac{R_g}{R_f} = 1$ for the cross-sections of both 90° (a) and 45° (b) struts.

shape defect description i.e. a better approximation of the strut real geometry. However, there is an existing number of modes beyond which the description accuracy is not improved anymore (see modes higher than 85 in Figure 8a). Higher number of modes even increases the resulting error due to high mode oscillations affecting the shape defect description, although it decreases the correlation score. As an example, mode 85 errors should be observed in Figure 8a and Figure 8b: mode 255, even supposed to provide a better shape description, results in higher errors than mode 85. Modes 85 and 125 provide with very similar errors. However, to preserve computational costs, 85 modes should be privileged as the higher modes, the longer computation time. 90° and the 45° struts required a computation time (CPU time) of respectively 103.2 s and 204.64 s in the 85 modes consideration, with the following hardware: Intel(R) Core(TM) i7-10850H CPU, 2.70 GHz, 16 Go RAM. It is worth noting that 45° strut requires more time due to the high deformation needed in comparison to the 90°. 105 modes required approximately 17% more time for both struts. Conversely, small number of modes does not sufficiently provide defect description (see for example mode 5 for both struts in Figure 8). That is why, in the following, 85 modes will be taken in consideration for further 2D V2C runs. This value is then an upper-bound of the number of modes that should be considered relative to the chosen defect basis for strut application of V2C.

Examination of modal participation bars (Figure 9) provides analytical tools to better understand mode dominance in the shape defect description amongst other modes. In fact, modal amplitude decreases with mode number as explained by Samper *et al.* [57]. Results show that both struts can be described with a small number of modes. In other words, low-level shape descriptors such

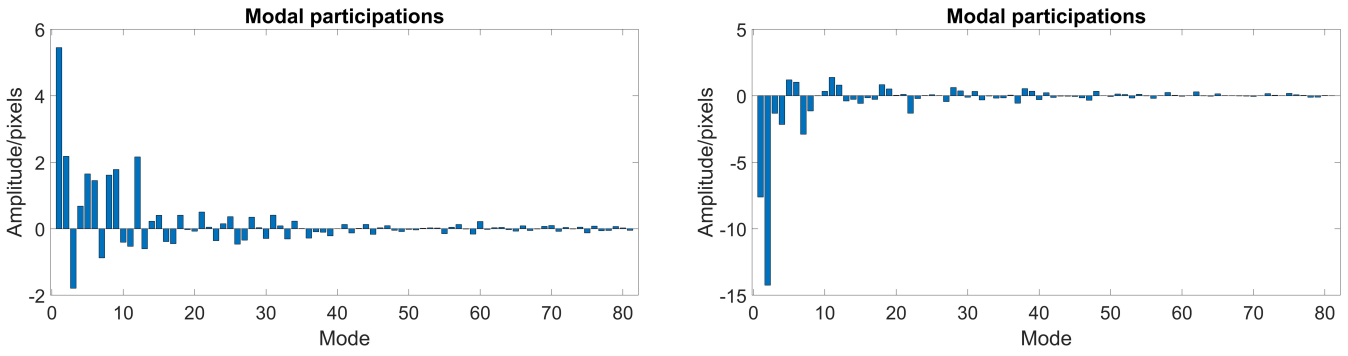

(a) (b)

Figure 9: Modal amplitude according to the considered modes for the cross-sections of 90 ° (a) and 45 ° (b) struts. Bandwidth R_g size has been optimally chosen to match $\frac{R_g}{R_f} = 1$ (registration modes have been removed in this figure).

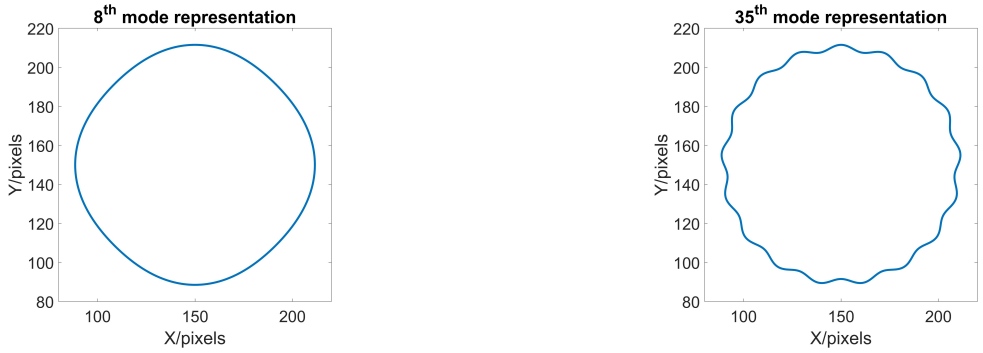

(a) (b)

Figure 10: Geometrical representation of 8^{th} (a) and 35^{th} mode (b) descriptions.

as the one represented in Figure 10a have more influence than wavy high-level shape descriptors such as the one represented in Figure 10b. For this 2D application of V2C, modal participation bars for both 45° and 90° struts might be categorised in three sets:

- High-impact modes which are the 20 first considered plane modes.
- Medium-impact modes, which are the plane modes between 20 and 45.
- Low-impact modes, which are beyond the 45^{th} plane modes

As previously mentioned, V2C relies on a matrix pseudo-inversion (see equation 10). Evaluation of conditioning values sampled at different stages of the correlation process shows values around 8 to 10 for both struts. Thus, with the chosen modal description, the 2D V2C is well-conditioned as lowest and highest M matrix eigen values have approximately the same impacts on the correlation.

4.3 Mode consideration for 3D V2C

V2C is applied for one strut belonging to each 90° and 45° sets relying on the aforementioned defect basis. Resulting vertical and plane modal participations are displayed in Figure 11. Whereas number of plane modes were taken accordingly to the sensitivity study presented in the previous section, taper, hourglass and five vertical modes are taken as vertical modes as a first approximation. This value has been taken as vertical defects are assumed to belonging to the five first vertical waviness such as pure flexion. Specific attention should be drawn to the modal amplitude for both struts. First of all, in both cases, pure flexion can be observed as of high importance in comparison to higher order vertical modes. The study could only consider taper, hourglass and about two vertical modes to accurately take the vertical defect into consideration. For plane modes, previous sections showed that considering 80 plane modes was a maximum for sufficiently representing shape defect. However, with the right parts of Figure 11a and 11b, the number of considered plane modes can be lowered even for 3D application of V2C. Indeed, for the 45° strut, shape defect is mainly elliptic as described in [54]. This elliptic property of the 45° strut is found by the main two first plane mode amplitudes displayed in Figure 11b, with amplitudes respectively of 52 μm and -23 μm, in comparison to higher frequency amplitudes. Indeed, back in their mathematical expressions defined in Section 2.3, these two first plane modes mathematically describe ellipse. Higher order modes certainly provide a

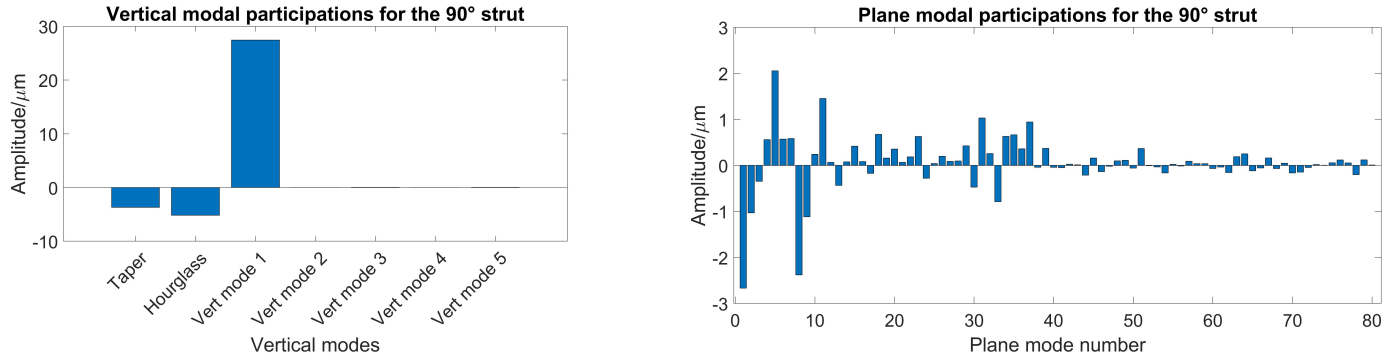

(a) 90° strut

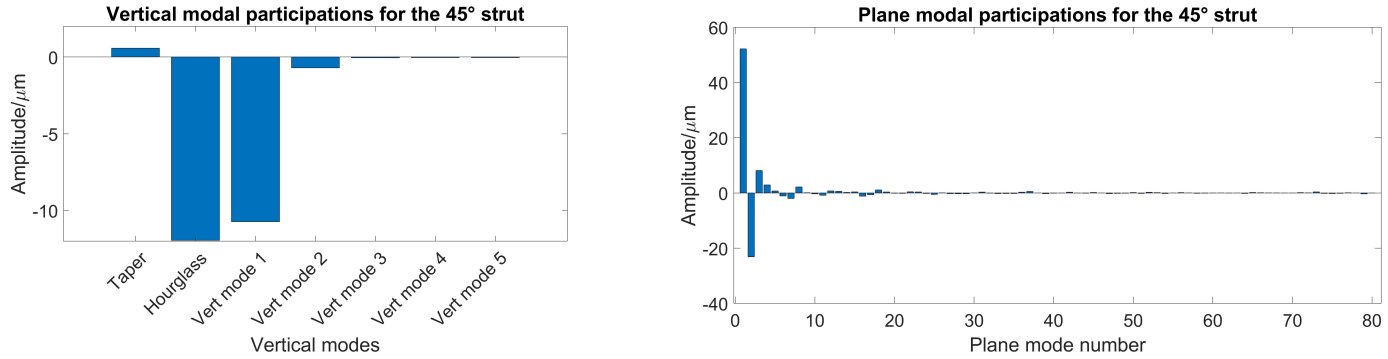

(b) 45° strut

Figure 11: Vertical (left) and plane (right) modal participations for the 90° (a) and the 45° (b) struts.

better shape defect information but with the observed decreasing amplitude, as explained in [57], this information has lower importance. Indeed, it seems that beyond 20 plane modes, amplitudes displayed in Figure 11 are under the micron for both struts and thus does not narrow the shape defect identification anymore. This 1 μm cut-off value was chosen to be consistent with the XCT resolution as 1 μm cut-off is approximately 10% of the XCT voxel size. Thus, considering 20 plane modes is largely sufficient to estimate these lattice struts shape defect. In the following, for 3D application, vertical modes would include taper, hourglass and two flexion modes, whereas 20 plane modes would be considered.

5 V2C validation study

In this section, 5 struts from each of the 90° and 45° are considered (see Figure 3). The aim of this section is to incorporate repeatability studies into this work.

5.1 Description of methodology

Each strut provides three point clouds:

- FV point clouds
- $ISO_{50\%}$ point clouds
- V2C point clouds

In this section, we highlight the coherence of V2C modal amplitudes regarding other measured dataset. That is why, a non-rigid registration [58] is separately applied on FV and $ISO_{50\%}$ point clouds relying on the same user-defined shape defect basis as the one considered for V2C and presented in Section 2. As outlined in the previous section, vertical modes are taken as taper, hourglass and two vertical flexion modes, whereas 20 plane modes will be considered. Outputs of these non-rigid registrations are modal amplitudes that can be compared all-together with modal amplitudes provided by V2C. Later, correlated, FV and $ISO_{50\%}$ shape defect envelopes are reconstructed relying on the modal amplitudes found respectively by V2C and by non-rigid registration performed on FV and $ISO_{50\%}$ point clouds. FV and $ISO_{50\%}$ shape defect envelopes are then separately compared to the correlated (by V2C) envelope with computation of mean, RMS errors and confidence intervals. Data processing pipeline is summarised in Figure 12.

5.2 Results for two struts

Summarising, results are firstly displayed and discussed for two struts, belonging to each 90° and 45° strut sets. In the next section, results will be extended to the entire sets, i.e. 10 struts in total, without displaying each of the figures presented hereafter. Figure 13 shows the amplitudes of modal participations computed respectively by V2C, and non-rigid registration of FV and $ISO_{50\%}$ point

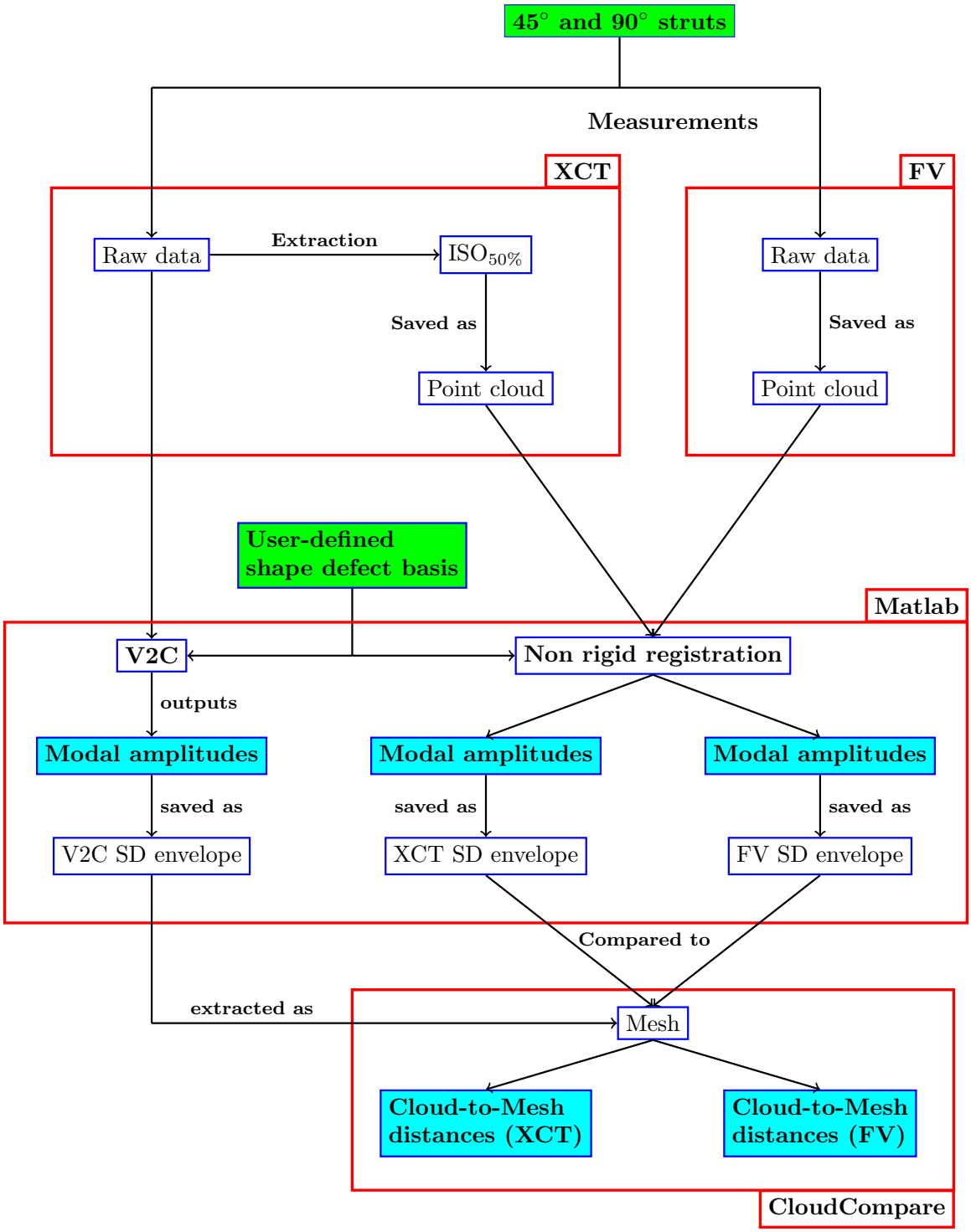

Figure 12: Data processing pipeline of V2C validation and comparison with non-rigid registration. Inputs are filled in green and outputs are filled in blue.

clouds. This figure allows us to compare the modal amplitude reached for each mode and to identify the consistency of V2C modal decomposition towards non-rigid registration upon the same shape defect basis. For the 90° strut, considering the relative low amplitudes, we can say that modal participation displayed for V2C, FV and XCT are similar. Again, the 90° strut is not significantly affected with shape defect. With amplitudes below the XCT resolution, discrepancies in the modal participation cannot be fully explained and stem most likely from numerical noise. For the 45° strut, vertical modal participations seem consistent for FV-registered and XCT-registered sets. However, discrepancies remain towards V2C vertical modal participation. Hence, modal participations would appear

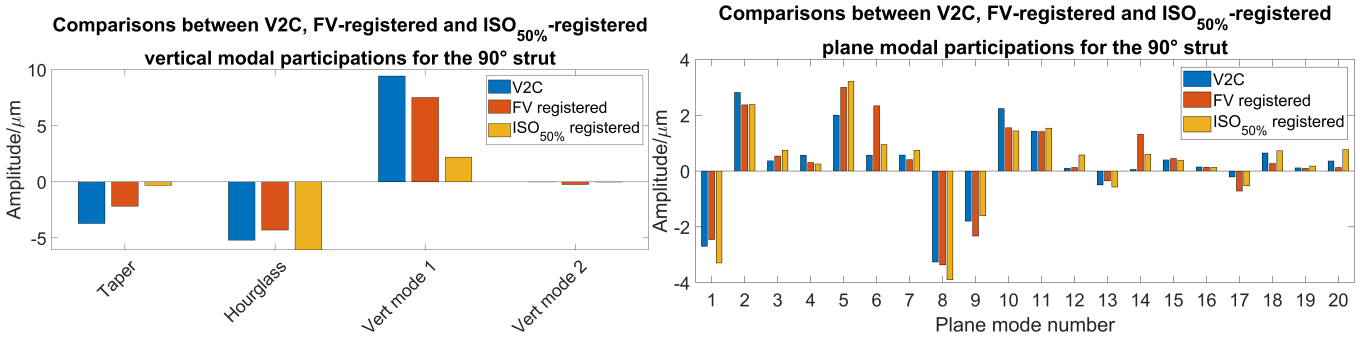

(a) 90° strut

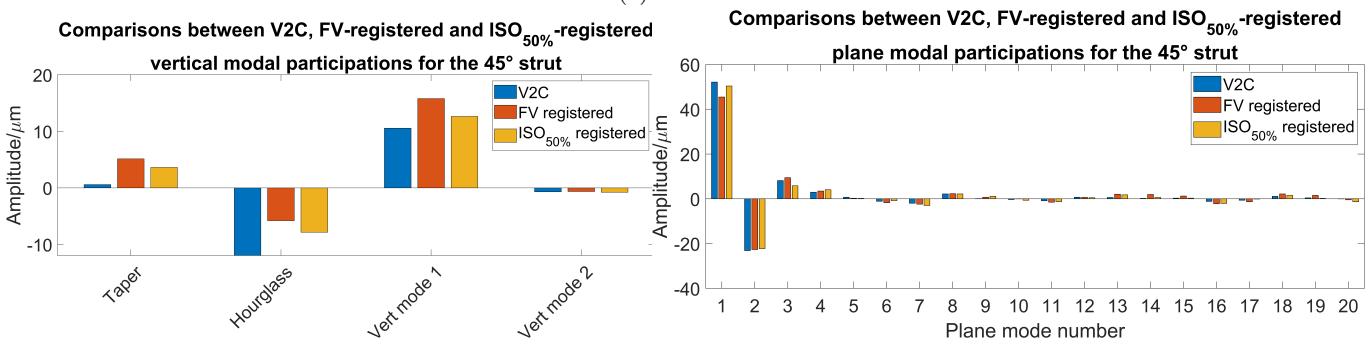

(b) 45° strut

Figure 13: Comparisons between V2C, FV-registered, $ISO_{50\%}$-registered vertical (left) and plane (right) modal participations for the 90° (a) and 45° (b) struts. Differences of plane mode amplitudes should be noted.

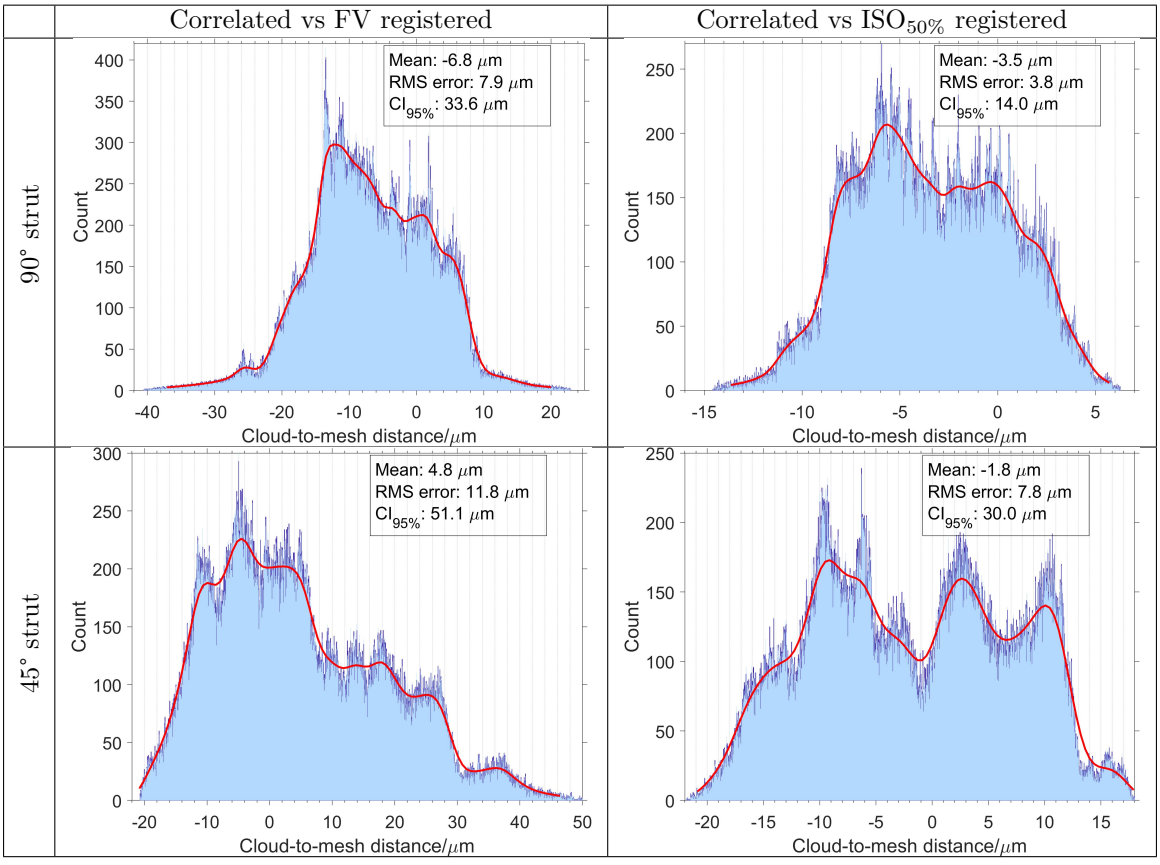

Figure 14: Reconstructed shape defect envelope comparisons between correlated (by V2C) and respectively FV-registered (left) and $ISO_{50\%}$-registered (right) for 90° and 45° struts.

to be in accordance for V2C and both registrations on the the first plane modes. Beyond the 4^{th} plane mode, amplitudes are too low and the interpretation falls below the XCT resolution. All in all, the high level of similarity between V2C and both registered modal participations can be outlined. Reconstructed shape defect

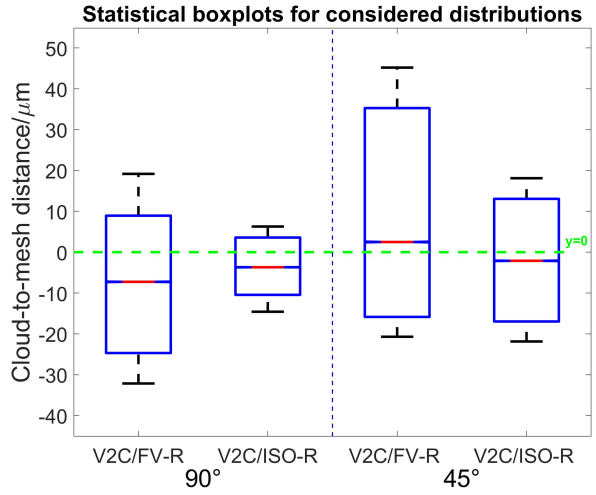

Figure 15: Statistical boxplots for considered comparative sets. For both 45° and 90° struts, V2C envelope is compared to the registered FV and ISO envelopes (FV-R and $ISO_{50\%}$-R respectively), green dashed line highlights the 0 value, blue boxes are the 95% CIs, upper and lower whiskers are the maximum and minimum values.

envelopes are compared to the correlated one and deviation distributions are displayed in Figure 14 where means, RMS errors and confidence intervals (CIs) of the means at 95% confidence, are indicated. Associated statistical boxplots are displayed in Figure 15, where 95% CIs are depicted by blue boxes and defined as the difference between 95.7% and 2.5% percentiles. Whiskers represent minimum and maximum values. As shown in both Figure 14 and 15, correlated vs FV registered envelopes results in wider distribution than correlated vs ISO registered for both struts. This observation may be explained by the sequence of FV data fusion. Indeed, FV measurement of the entire strut required multiple fusions of ROI in the manufacturer's software. The latter may have introduced registration errors that are combined leading to an overall error. Results also show that for both of the chosen 90° and 45° struts, and both comparative sets (either correlated vs FV-registered or correlated vs $ISO_{50\%}$-registered), RMS errors are below 12 μm. More precisely, RMS errors are even below 8 μm for the 90° strut, i.e. below the voxel resolution of the XCT measurement. Indeed, previous sections highlighted the small shape defect contained in vertical struts. This has been shown by small modal amplitudes, and could be explained by the manufacturing contouring strategy which reduces shape defect deviations. Increased RMS errors for the 45° strut can be explained by its surface topography. During the manufacturing process, down-facing surfaces of 45° struts have no supporting structures, resulting in poor strut surface quality. These rough surfaces impact XCT and FV measurements and thus V2C as well as non-rigid registrations in the shape defect identification. Conversely, 90° struts are built vertically and do not require supporting structure. In addition, the manufacturing step includes a contouring strategy which drastically improves the 90° strut surface quality. Finally, the wide difference between minimum and maximum values for the 45° strut should be outlined. Deviations are indeed wider than the 90° strut and are also explained by the poor surface quality of 45° struts: V2C provides with an overall shape defect and does not account for lower wavelength defects.

5.3 Extension to several struts

In this section, the aforementioned methodology is applied on the ten printed 90° and 45° struts (see Figure 3). Figure 16 presents the computed RMS errors between correlated and reconstructed shape defect envelopes for both FV and $ISO_{50\%}$ non-rigid registrations. Results show significant consistency along the comparative sets. This observation highlights the robustness of V2C and the chosen modal basis towards spatially-repeated printed struts. As previously explained, 45° struts present poorer surface quality than 90° struts due to the combined effects of supporting structure impact on the resulting strut surface roughness and the laser scanning strategy. All in all, Figure 16 shows that RMS errors for all comparative sets are in the same order as the XCT measurement resolution, and even lower for 90° struts. RMS errors are relatively low considering the aim to estimate strut shape defect. Thereby, displayed results show the consistency of V2C over spatially repeated struts. In addition, regarding strut shape defect, V2C provides with the same quality of information as non-rigid registrations stemming from FV measurement or $ISO_{50\%}$ extraction.

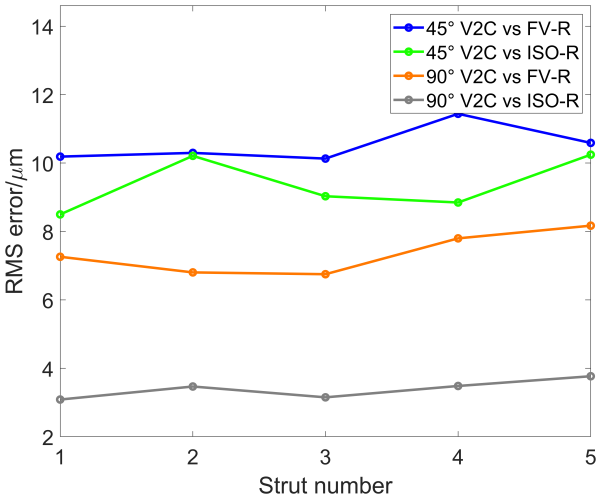

Figure 16: RMS errors between correlated (V2C) envelopes towards registered FV envelope (FV-R) and $ISO_{50\%}$ envelope (ISO-R), relative to the strut typology.

5.4 Repeatability studies

In this section, measurement repeatability relative to 3D V2C is investigated. A 45° strut and a 90° strut are considered in the following. Each strut is measured consecutively 5 times by XCT with the same instrument parameters described in section 3.2. 3D V2C is applied on each of the repeated measurements relative to the same shape defect basis, and modal amplitudes are identified for each measured strut. Thereby, for each of the two struts, the five sets of modal amplitudes allow the mean amplitude to be computed for each mode. CI for the mean amplitude is estimated for each mode relying on t-distributions at 95% confidence. T-distributions are used instead of Gaussian distributions because of the small sample size considered for each mode, made of 5 amplitude values. Figure 17a (resp. 17b) displays the 90° strut (resp. 45° strut) CI widths on the mean at 95% confidence. The choice to display CI widths was made to focus the observation on CI width rather than on amplitude value. Such a representation allows comparisons between modes to be performed as amplitudes may be very different from a strut to another, as well as from a mode to another. Indeed, as previously explained, amplitudes naturally decrease with the number of considered plane modes. That is why, combining on a same plot mean values as well as CIs is not relevant, the range of involved scales being too wide. Statistical discrepancy is then seen for all modal amplitudes considered in each strut. Results show that CIs are relatively narrow for each mode, about 0.3 μm for the 90° strut and about 3 μm for the 45° strut. In other words, the 45° strut show poorer repeatability than the 90° strut. This may be explained by the surface topography of the 45° strut affecting the XCT measurement implying a correlation between measurement repeatbility and the nature of strut. Previous work [68] outlined high-slope features affecting XCT uncertainty. This result was not especially expected for the volumetric nature of XCT, that is why, investigations are still required to understand that observed correlation. For plane modes, it seems that CI width decreases with the number of mode. However, amplitude decrease with number of mode should be reminded and high number of plane mode are less expressed than the first plane modes. Taper and hourglass, are the modes with obviously the wider CIs in both struts. This observation may be explained by the confusion V2C may have between registration modes such as small rotations or translations, with taper or hourglass modes. All in all, vertical modes seem to have wider CIs than plane modes. This may be explained by the smoothing property of V2C being dominant on plane modes. In details, the same plane mode is defined at each altitude of the strut resulting in the smoothing effect of very local defects such as spatters. Vertical defects, by definition (see Figure 2) are defined once and depend on the vertical position. Thus, V2C is more robust in mode determination with plane modes than with vertical modes.

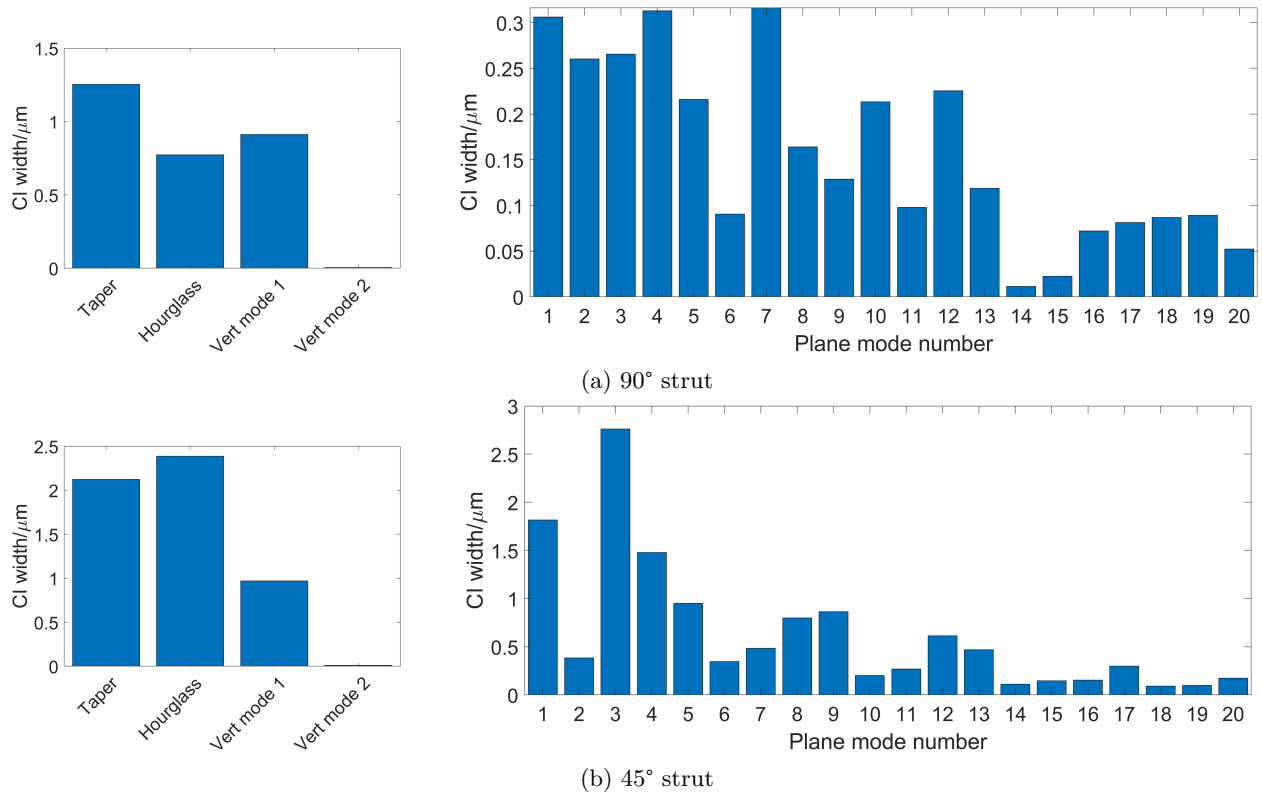

(a) 90° strut

(b) 45° strut

Figure 17: Statistical modal amplitude CI widths computed for the 90° strut (a) and the 45° strut (b). CIs with a 95% confidence are computed relying on T-distributions. Amplitude ranges should be outlined.

5.5 Discussion

In this work, V2C and registrations have been performed relative to the same user-defined shape defect basis for a purpose of consistency. RMS errors between correlated and registered envelopes being in the same order highlight the similarity of information extracted by V2C, registered FV or registered $ISO_{50\%}$ regarding the shape defect basis. Thus, V2C can be used as an efficient shape defect extraction tool which does not require surface determination and further data treatment handling. Nevertheless, to correctly represent shape defect, it is worth questioning the chosen shape defect basis. Based on literature and the results presented in this paper, the proposed shape defect basis is quite representative of the expected strut shape defect. However, strut surface also presents local stochastic defects such as spatters or local recesses, which are not expressed on the entire strut length. With the chosen shape defect basis, V2C performs a smoothing effect of these very local defects which have not been described in the defect basis. Although the chosen shape defect basis does not account for higher wavelength defects, integrating these stochastic defects into V2C would be interesting to perform.
Repeatability studies presented herein include spatial repeatability of lattice struts as well as XCT measurement repeatability for the V2C application. Results highlight the V2C consistency and robustness towards considered studies. Regarding shape defect, V2C provides with the same quality of information and can be considered as an efficient shape defect extraction tool. Lower wavelength defects, and stochastic defects introduced whilst manufacturing such as spatters, are not identified by V2C in its present form as the considered defect descriptors only focus on shape defects. Measurement repeatability study also identified a correlation between the nature of considered strut and CI width. Investigations are still required to deepen the XCT uncertainty understanding to limit its impact on V2C
Then, although this work involves many data stemming from different measurement techniques acquired by skilled operators, improvement are always possible that could decrease registration time or convergence speed. Indeed, V2C involves volumetric data treatments and thus requires specific RAM needs. In the V2C presented in this paper, not less than 110 gigabytes of RAM were needed on a high performance computing cluster. Finally, V2C has the advantage of providing the user with strut shape defect information directly from volumetric data. As a result, shape defect identification with V2C doesn't require neither surface determination nor additional user-dependant steps such as meshing and registration, prior to dimensional assessments relative to the CAD nominal model. In other words, uncertainty sources are restrained and the CAD model can be directly updated with the identified information from volumetric data. This direct link between volumetric data and the CAD model raises new comprehensive stakes that will be the object of further work.

6 Conclusion

V2C has been presented in order to describe strut-based lattice beam shape defects as V2C provides with better defect information than least square cylinder approximations. The proposed method allows the strut shape defect to be expressed as a sum of modal participation relying on the user-defined defect basis. Optimal parameters such as virtual image bandwidth or number of modes to consider are found in a 2D validation study. Extended to 3D, the V2C method allows volumetric shape defects to be digitally reconstructed directly from XCT measurements. This work highlights the suitability of V2C to identify strut shape defect with the considered defect basis, as well as non-rigid registration from FV measurements or $ISO_{50\%}$ extractions. Future work will continue to focus on adapting this V2C methodology to more complex AM structures such as whole lattice structures or complex geometries obtained by topological optimisation. The entire lattice structure raises the scale of shape defect challenge. Significant efforts should then be invested in precisely characterising the geometric representation by taking more parameters into consideration without compromising the numerical optimisation problem.

Acknowledgements

- CT measurements at ENS Paris-Saclay have been financially supported by the French *Agence Nationale de la Recherche*, through the *Investissements d'avenir* program (ANR-10-EQPX-37 MATMECA Grant)

- This work was performed using HPC resources from the *Mésocentre* computing center of CentraleSupélec and École Normale Supérieure Paris-Saclay supported by CNRS and Région Île-de-France (http://mesocentre.centralesupelec.fr)

References

[1] I. I. Gibson, *Additive manufacturing technologies : 3D printing, rapid prototyping, and direct digital manufacturing / Ian Gibson, David Rosen, Brent Stucker*. New York: Springer, 2nd ed. ed., 2015.

[2] K. K. B. Hon, "Digital additive manufacturing: From rapid prototyping to rapid manufacturing," in *Proceedings of the 35th International MATADOR Conference* (S. Hinduja and K.-C. Fan, eds.), (London), pp. 337–340, Springer London, 2007.

[3] R. Hasan, R. Mines, E. Shen, S. Tsopanos, W. Cantwell, W. Brooks, and C. Sutcliffe, "Comparison of the drop weight impact performance of sandwich panels with aluminium honeycomb and titanium alloy micro lattice cores," *Applied Mechanics and Materials*, vol. 24, pp. 413–418, 06 2010.

[4] Y. Shen, W. Cantwell, R. Mines, and Y. Li, "Low-velocity impact performance of lattice structure core based sandwich panels," *Journal of Composite Materials*, vol. 48, pp. 3153–3167, 09 2013.

[5] D. Haack, K. Butcher, T. Kim, and T. Lu, "Novel lightweight metal foam heat exchangers," *American Society of Mechanical Engineers, Process Industries Division (Publication) PID*, vol. 6, 01 2001.

[6] C. S. Roper, K. D. Fink, S. T. Lee, J. A. Kolodziejska, and A. J. Jacobsen, "Anisotropic convective heat transfer in microlattice materials," *AIChE Journal*, vol. 59, no. 2, pp. 622–629, 2013.

[7] I. Echeta, X. Feng, B. Dutton, S. Piano, and R. Leach, "Review of defects in lattice structures manufactured by powder bed fusion," *International Journal of Advanced Manufacturing Technology*, vol. 106, 01 2020.

[8] B. Lozanovski, M. Leary, P. Tran, D. Shidid, M. Qian, P. Choong, and M. Brandt, "Computational modelling of strut defects in slm manufactured lattice structures," *Materials & Design*, vol. 171, p. 107671, 2019.

[9] T. B. Sercombe, X. Xu, V. Challis, R. Green, S. Yue, Z. Zhang, and P. D. Lee, "Failure modes in high strength and stiffness to weight scaffolds produced by selective laser melting," *Materials & Design*, vol. 67, pp. 501 – 508, 2015.

[10] E. Abele, H. A. Stoffregen, K. Klimkeit, H. Hoche, and M. Oechsner, "Optimisation of process parameters for lattice structures," *Rapid Prototyping Journal*, 2015.

[11] A. Hadi, F. Vignat, and F. Villeneuve, "Design Configurations and Creation of Lattice Structures for Metallic Additive Manufacturing," in *14ème Colloque National AIP PRIMECA*, (La Plagne, France), Mar. 2015.

[12] C. Beyer and D. Figueroa, "Design and analysis of lattice structures for additive manufacturing," *Journal of Manufacturing Science and Engineering*, vol. 138, 06 2016.

[13] AMT/8, *BS EN ISO/ASTM 52900:2017 - Additive manufacturing. General principles. Terminology.* 2016.

[14] B. Zhang, Y. Li, and Q. Bai, "Defect formation mechanisms in selective laser melting: A review," *Chinese Journal of Mechanical Engineering*, vol. 30, pp. 515–527, 03 2017.

[15] C. Galy, E. L. Guen, E. Lacoste, and C. Arvieu, "Main defects observed in aluminum alloy parts produced by slm: From causes to consequences," *Additive manufacturing*, vol. 22, pp. 165–175, 2018.

[16] E. Malekipour and H. El-Mounayri, "Common defects and contributing parameters in powder bed fusion am process and their classification for online monitoring and control: a review," *The International Journal of Advanced Manufacturing Technology*, vol. 95, 03 2018.

[17] T. Vo, M. Museau, F. Vignat, F. Villeneuve, Y. Ledoux, and A. Ballu, "Typology of geometrical defects in electron beam melting," *Procedia CIRP*, vol. 75, pp. 92 – 97, 2018. The 15th CIRP Conference on Computer Aided Tolerancing, CIRP CAT 2018, 11-13 June 2018, Milan, Italy.

[18] L. Liu, P. Kamm, F. García-Moreno, J. Banhart, and D. Pasini, "Elastic and failure response of imperfect three-dimensional metallic lattices: the role of geometric defects induced by selective laser melting," *Journal of the Mechanics and Physics of Solids*, vol. 107, pp. 160–184, 2017.

[19] Y. Amani, S. Dancette, P. Delroisse, A. Simar, and E. Maire, "Compression behavior of lattice structures produced by selective laser melting: X-ray tomography based experimental and finite element approaches," *Acta Materialia*, vol. 159, pp. 395–407, 2018.

[20] Z. Alomar and F. Concli, "A review of the selective laser melting lattice structures and their numerical models," *Advanced Engineering Materials*, vol. 22, no. 12, p. 2000611, 2020.

[21] K. Ferreira, N. Anwer, and C. Mehdi-Souzani, "Characterization of l-pbf lattice structures geometric defects," *Procedia CIRP*, vol. 100, pp. 846–851, 2021. 31st CIRP Design Conference 2021 (CIRP Design 2021).

[22] B. Lozanovski, D. Downing, R. Tino, A. du Plessis, P. Tran, J. Jakeman, D. Shidid, C. Emmelmann, M. Qian, P. Choong, *et al.*, "Non-destructive simulation of node defects in additively manufactured lattice structures," *Additive Manufacturing*, vol. 36, p. 101593, 2020.

[23] I. Echeta, B. Dutton, R. K. Leach, and S. Piano, "Finite element modelling of defects in additively manufactured strut-based lattice structures," *Additive Manufacturing*, p. 102301, 2021.

[24] N. Korshunova, G. Alaimo, S. Hosseini, M. Carraturo, A. Reali, J. Niiranen, F. Auricchio, E. Rank, and S. Kollmannsberger, "Image-based numerical characterization and experimental validation of tensile behavior of octet-truss lattice structures," *Additive Manufacturing*, vol. 41, p. 101949, 2021.

[25] J. Réthoré and M. François, "Curve and boundaries measurement using b-splines and virtual images," *Optics and Lasers in Engineering*, vol. 52, pp. 145 – 155, 2014.

[26] Z. Y. Chua, I. H. Ahn, and S. K. Moon, "Process monitoring and inspection systems in metal additive manufacturing: Status and applications," *International Journal of Precision Engineering and Manufacturing-Green Technology*, vol. 4, no. 2, pp. 235–245, 2017.

[27] L. Chiffre, S. Carmignato, J.-P. Kruth, R. Schmitt, and A. Weckenmann, "Industrial applications of computed tomography," *CIRP Annals - Manufacturing Technology*, vol. 63, 12 2014.

[28] A. Thompson, D. McNally, I. Maskery, and R. K. Leach, "X-ray computed tomography and additive manufacturing in medicine: a review," *International Journal of Metrology and Quality Engineering*, vol. 8, p. 17, 2017.

[29] A. Thompson, I. Maskery, and R. K. Leach, "X-ray computed tomography for additive manufacturing: a review," *Measurement Science and Technology*, vol. 27, p. 072001, jun 2016.

[30] F. H. Kim, A. L. Pintar, S. P. Moylan, and E. J. Garboczi, "The influence of x-ray computed tomography acquisition parameters on image quality and probability of detection of additive manufacturing defects," *Journal of manufacturing science and engineering*, vol. 141, no. 11, p. 111002, 2019.

[31] J. S. Rathore, C. Vienne, Y. Quinsat, and C. Tournier, "Influence of resolution on the x-ray ct-based measurements of metallic am lattice structures," *Welding in the World*, vol. 64, pp. 1367–1376, 2020.

[32] Ángela Rodríguez-Sánchez, A. Thompson, L. Körner, N. Brierley, and R. Leach, "Review of the influence of noise in x-ray computed tomography measurement uncertainty," *Precision Engineering*, vol. 66, pp. 382–391, 2020.

[33] F. Zanini, M. Sorgato, E. Savio, and S. Carmignato, "Dimensional verification of metal additively manufactured lattice structures by x-ray computed tomography: Use of a newly developed calibrated artefact to achieve metrological traceability," *Additive Manufacturing*, vol. 47, p. 102229, 2021.

[34] M. Praniewicz, M. Ferrucci, J. Fox, C. Saldana, *et al.*, "Testing the similarity conditions in the ct measurement of additively manufactured lattice structures," in *Proceedings of the Joint Special Interest Group meeting between euspen and ASPE Advancing Precision in Additive Manufacturing*, 2021.

[35] W. Dewulf, K. Kiekens, Y. Tan, F. Welkenhuyzen, and J.-P. Kruth, "Uncertainty determination and quantification for dimensional measurements with industrial computed tomography," *CIRP Annals*, vol. 62, no. 1, pp. 535 – 538, 2013.

[36] J. J. Lifton, A. A. Malcolm, and J. W. McBride, "On the uncertainty of surface determination in x-ray computed tomography for dimensional metrology," *Measurement Science and Technology*, vol. 26, p. 035003, feb 2015.

[37] J. Yague-Fabra, S. Ontiveros, R. Jimanez, S. Chitchian, G. Tosello, and S. Carmignato, "A 3d edge detection technique for surface extraction in computed tomography for dimensional metrology applications," *CIRP Annals*, vol. 62, no. 1, pp. 531 – 534, 2013.

[38] S. Carmignato, "Accuracy of industrial computed tomography measurements: experimental results from an international comparison," *CIRP annals*, vol. 61, no. 1, pp. 491–494, 2012.

[39] J. P. Kruth, M. Bartscher, S. Carmignato, R. Schmitt, L. De Chiffre, and A. Weckenmann, "Computed tomography for dimensional metrology," *CIRP annals*, vol. 60, no. 2, pp. 821–842, 2011.

[40] L. Ding and A. Goshtasby, "On the canny edge detector," *Pattern Recognition*, vol. 34, no. 3, pp. 721–725, 2001.

[41] S. Lou, W. Sun, W. Zeng, L. Pagani, X. Jiang, and P. Scott, "Development of 2d local searching algorithms for surface determination of x-ray computed tomography measurement," in *3rd Dimensional X-ray Computed Tomography Conference, University of Nottingham*, 07 2018.

[42] F. B. de Oliveira, A. Stolfi, M. Bartscher, L. De Chiffre, and U. Neuschaefer-Rube, "Experimental investigation of surface determination process on multi-material components for dimensional computed tomography," *Case studies in nondestructive testing and evaluation*, vol. 6, pp. 93–103, 2016.

[43] J. López and C. Vila, "An approach to reverse engineering methodology for part reconstruction with additive manufacturing," in *IOP Conference Series: Materials Science and Engineering*, vol. 1193, p. 012047, IOP Publishing, 2021.

[44] M. L. M. François, A. Bloch, and J. C. Thomas, "Metrology of contours by the virtual image correlation technique," in *Advancement of Optical Methods in Experimental Mechanics, Volume 3* (H. Jin, S. Yoshida, L. Lamberti, and M.-T. Lin, eds.), (Cham), pp. 239–246, Springer International Publishing, 2016.

[45] F. Hild and S. Roux, "Digital Image Correlation: From Displacement Measurement to Identification of Elastic Properties - A Review," *Strain*, vol. 42, no. 2, pp. 69–80, 2006.

[46] B. Semin, H. Auradou, and M. François, "Accurate measurement of curvilinear shapes by virtual image correlation," *The European Physical Journal Applied Physics*, vol. 56, 10 2011.

[47] A. Bloch, M. François, J.-C. Thomas, and O. Flamand, "Monitoring of Inflatable Structures by Using Virtual Image Correlation," in *EWSHM - 7th European Workshop on Structural Health Monitoring* (L. Cam, Vincent, Mevel, Laurent, Schoefs, and Franck, eds.), (Nantes, France), IFFSTTAR, Inria, Université de Nantes, July 2014.

[48] Z. Jiang, J.-f. Witz, P. Lecomte-Grosbras, J. Dequidt, C. Duriez, M. Cosson, S. Cotin, and M. Brieu, "B-spline based multi-organ detection in magnetic resonance imaging: B-spline based multi-organ detection in mri," *Strain*, vol. 51, 04 2015.

[49] Z. Jiang, O. Mayeur, J.-F. Witz, P. Lecomte-Grosbras, J. Dequidt, M. Cosson, C. Duriez, and M. Brieu, "Virtual image correlation of magnetic resonance images for 3d geometric modelling of pelvic organs," *Strain*, vol. 55, no. 3, p. e12305, 2019. e12305 10.1111/str.12305.

[50] M. Kunt, "Edge detection : A tuttorial review," in *ICASSP '82. IEEE International Conference on Acoustics, Speech, and Signal Processing*, vol. 7, pp. 1172–1175, IEEE, 1982.

[51] B. Magnier, H. Abdulrahman, and P. Montesinos, "A review of supervised edge detection evaluation methods and an objective comparison of filtering gradient computations using hysteresis thresholds," *Journal of Imaging*, vol. 4, no. 6, 2018.

[52] B. Magnier, "Edge detection: a review of dissimilarity evaluations and a proposed normalized measure," *Multimedia Tools and Applications*, vol. 77, no. 8, pp. 9489–9533, 2018.

[53] Dharampal and V. Mutneja, "Methods of image edge detection: A review," *Journal of Electrical & Electronic Systems*, vol. 04, 01 2015.

[54] J. S. Rathore, C. Mang, C. Vienne, Y. Quinsat, and C. Tournier, "A methodology for computed tomography-based non-destructive geometrical evaluations of lattice structures by holistic strut measurement approach," *Journal of Manufacturing Science and Engineering*, vol. 143, no. 5, p. 051012, 2021.

[55] M. Radouani and B. Anselmetti, "Identification of real surfaces and inspection of the iso specifications using a solver," *Mech. Ind.*, pp. 249–258, 2003.

[56] A. Alghamdi, T. Maconachie, D. Downing, M. Brandt, M. Qian, and M. Leary, "Effect of additive manufactured lattice defects on mechanical properties: an automated method for the enhancement of lattice geometry," *The International Journal of Advanced Manufacturing Technology*, vol. 108, no. 3, pp. 957–971, 2020.

[57] S. Samper and F. Formosa, "Form defects tolerancing by natural modes analysis," *Journal of Computing and Information Science in Engineering*, vol. 7, no. 1, pp. 44–51, 2007.

[58] F. Thiébaut, S. Bendjebla, Y. Quinsat, and C. Lartigue, "Non-rigid registration for form defect identification of thin parts," *Journal of Computing and Information Science in Engineering*, vol. 18, no. 2, 2018.

[59] L. Homri, E. Goka, G. Levasseur, and J.-Y. Dantan, "Tolerance analysis: Form defects modeling and simulation by modal decomposition and optimization," *Computer-Aided Design*, vol. 91, 06 2017.

[60] G. L. Goic, H. Favreliere, S. Samper, and F. Formosa, "Multi scale modal decomposition of primary form, waviness and roughness of surfaces," *Scanning*, vol. 33, no. 5, pp. 332–341, 2011.

[61] D. Etievant, Y. Quinsat, F. Thiebaut, and F. Hild, "A modal approach for shape defect measurement based on global stereocorrelation," *Optics and Lasers in Engineering*, vol. 128, p. 106030, 2020.

[62] J. A. Sethian, *Level set methods and fast marching methods : evolving interfaces in computational geometry, fluid mechanics, computer vision, and materials science / J.A. Sethian.* Cambridge monographs on applied and computational mathematics ; 3, Cambridge: Cambridge University Press, 2nd ed. ed., 1999.

[63] *NF EN ISO/ASTM 52902:2019 - Additive manufacturing - Test artifacts - Geometric capability assessment of additive manufacturing systems.* 2019.

[64] M.-A. de Pastre, S.-C. Toguem Tagne, and N. Anwer, "Test artefacts for additive manufacturing: A design methodology review," *CIRP Journal of Manufacturing Science and Technology*, vol. 31, pp. 14 – 24, 2020.

[65] *BS EN ISO 25178-606:2015: Geometrical product specification (GPS). Surface texture: Areal. Nominal characteristics of non-contact (focus variation) instruments.* British Standards Institute, 2015.

[66] A. Townsend, R. Racasan, R. Leach, N. Senin, A. Thompson, A. Ramsey, D. Bate, P. Woolliams, S. Brown, and L. Blunt, "An interlaboratory comparison of x-ray computed tomography measurement for texture and dimensional characterisation of additively manufactured parts," *Additive Manufacturing*, vol. 23, pp. 422–432, 2018.

[67] N. Senin, A. Thompson, and R. K. Leach, "Characterisation of the topography of metal additive surface features with different measurement technologies," *Measurement Science and Technology*, vol. 28, p. 095003, aug 2017.

[68] M.-A. de Pastre, A. Thompson, Y. Quinsat, J. A. A. García, N. Senin, and R. Leach, "Polymer powder bed fusion surface texture measurement," *Measurement Science and Technology*, vol. 31, p. 055002, jan 2020.

[69] "Mathworks 2020 Matlab 2020a." https://fr.mathworks.com/products/matlab.html. Accessed: 2021-06-10.

[70] "Cloudcompare." http://www.cloudcompare.org. Accessed: 2021-06-10.

[71] Y. Tian, D. Tomus, P. Rometsch, and X. Wu, "Influences of processing parameters on surface roughness of hastelloy x produced by selective laser melting," *Additive Manufacturing*, vol. 13, pp. 103–112, 2017.

[72] K. Kiekens, F. Welkenhuyzen, Y. Tan, P. Bleys, A. Voet, J.-P. Kruth, and W. Dewulf, "A test object with parallel grooves for calibration and accuracy assessment of industrial computed tomography (CT) metrology," *Measurement Science and Technology*, vol. 22, p. 115502, sep 2011.

[73] "Fiji Image J." https://imagej.net/Welcome. Accessed: 2021-06-10.